THESIS FOR THE DEGREE OF DOCTOR OF PHILOSOPHY

Solar gasification in dual fluidized bed using solids as heat carrier

MONTSERRAT SUÁREZ ALMEIDA

Departamento de Ingeniería Química y Ambiental
Escuela Superior de Ingeniería, Universidad de Sevilla

Sevilla, España 2022

This work has been financed by the Spanish National Plan I+D+i in the frame of the NetuWas project (CTM2016-78089-R) and the Foundation Seed Fund MIT-Spain “la Caixa” with the SOLGASBI project. The author has been granted by Ministerio de Economía, Industria y Competitividad of Spanish government (BES-2017-080653) under the call “Ayudas para Contratos Predoctorales 2017” financed together FSE.

To my sister.

To my mother.

I will not have life to pay you.

Abstract

Biomass steam gasification assisted by concentrated solar energy is an attractive technology for the production of storable renewable energy and the reduction of CO_2 emissions. However, several challenges have stalled its deployment over the last decades: high temperature and/or large reactor volume required for complete fuel (char) conversion, the achievement of a steady syngas generation independent of solar radiation variation, and accomplishing effective heat supply at high temperature in large-scale reactors. This thesis deals with the analysis and design of a new scalable process to carry out the solar steam gasification overcoming the mentioned technical challenges.

This thesis proposes a new concept of biomass gasification assisted by solar thermal energy, as an extension of the state-of-the-art dual fluidized bed gasification (DFBG). In the process the gasification unit in the DFBG is not only heated by the solids coming from the combustion unit, but also by an external stream of solids that has been previously heated in a solar particle receiver. This configuration allows uncoupling the solar receiver and the reactor using a thermal energy storage (TES), while the thermal integration is highly efficient since carrier particles are directly used in the reactor. The reactor will operate with high share of solar external heat when available, while it will send more char to the combustor when the fraction of solar external heat decreases (at nights or during winter time).

A model of the proposed solar DFBG (SDFBG) was developed and used to assess the performance of the system. The results show that char conversion of 70–80% is a compromise for having a significant solar share in the syngas (around 12 %, defined as the fraction of chemical energy in the product gas coming from the solar energy) while maintaining reasonable gasifier volume i.e., char residence time in the range of 20-30 min. This operation is far from those of existing DFBG, using a much smaller gasifier volume, with limited residence time (1-5 min) and extent of char conversion (10-30%). Different integrations for the external solids circulation into the DFBG system were studied and, two of them were identified as the most advantageous for implementation in the process. The required solids circulations for the operation at high solar share resulted similar to those reported from existing DFBGs but, the required solids inventory for that operation is typically ten times higher than that in conventional DFBGs. As a result, current DFBGs should be significantly modified to allow the operation both in solar mode and autothermal conditions.

The new features imposed by the operation of the SDFBG require from a precise understanding of the fluid-dynamics of the system. A model of a conventional DFBG is developed to understand the hydrodynamic performance of current units, and then to extend the knowledge to solar conditions. The cold flow model (CFM) at TU-Wien, one of the pioneering CFM developed for studying the fluid-dynamics performance of DFBGs, is taken as reference and, experimental measurements from this unit are compared with the model results. The model was used to preliminary assess the fluid-dynamic characteristics of SDFBGs. The results show that typical solids inventories and solids fluxes required by an SDFBG can be achieved by increasing around three times the diameter of the gasification unit compared to that of a conventional DFBG. Moreover, the loop seal is identified as a key element for allowing the flexible operation of the SDFBG under different external heat loads.

Motivated by the key role of loop seal unit in the SDFBG, experimental work was carried out in an isolated loop seal CFM, intended to shed light on the fluid-dynamics of these units and, looking for fundamental knowledge to improve the current semi-empirical models. Results from the study show that the resistance offered by the horizontal passage (opening) of the loop seal, leads to non-homogeneous gas-solids flow pattern which, ultimately, establishes the fluid-dynamic performance of the unit. The non-ideal gas-solids flow patterns occurring in actual loop seals were demonstrated not to be addressed by simple semi-empirical 1D models, needing more complex computational

models to capture the 2D/3D effects. Although CFD is a useful tool to predict the behavior of these units, a comprehensive generalization is difficult; conclusions from this work can be useful to understand different designs.

All the gained knowledge was gathered and used to design a flexible SDFBG able to operate both under autothermal and at high allothermal conditions. The previously identified most advantageous integration options of the external solids circulation into the DFBG were considered, leading to different design and operation requirements. Char conversions in the gasifier from autothermal to high allothermal operation ranges from 15 to 80%, respectively, while the maximum solar external heat load rounds 2.6 $MJ/kg_{bio,daf}$ (typically 14% of the heating value of the biomass). This contrasts with the maximum share calculated by equilibrium (≈5 $MJ/kg_{bio,daf}$), indicating that there is still room for improvement if operating conditions in the gasifier are optimized.

Overall, the work clearly demonstrates that the proposed SDFBG presents huge scale up potential, taking the most of current state-of-the-art technologies of DFBG after some modifications, mainly: a wider gasifier unit, a narrower riser-combustor and a dedicated lower loop seal for adapting the operation to changes in external heat loads. Moreover, reactor optimization measures such as the combination of the developed solar DFBG with catalytic gasification and addition of sorbent to capture CO_2 seem to be promising extensions to provide even further benefits.

Keywords: steam gasification, solar energy, dual fluidized bed gasifier, fluid-dynamics, loop seal

List of publications

This thesis is based on the following papers, which are referred to in the text by their Roman numerals,

I. A. Gómez-Barea, M. Suárez-Almeida, A. Ghoniem. Analysis of fluidized bed gasification of biomass assisted by solar-heated particles. Biomass Conversion and Biorefinery 11(2021) 143–158. https://doi.org/10.1007/s13399-020-00865-0.

II. M. Suárez-Almeida, A. Gómez-Barea, A.F. Ghoniem, C. Pfeifer. Solar gasification of biomass in a dual fluidized bed. Chemical Engineering Journal 406 (2021) 126665. https://doi.org/10.1016/j.cej.2020.126665.

III. M. Suárez-Almeida, A. Gómez-Barea, C. Pfeifer, B. Leckner. Fluid dynamic analysis of dual fluidized bed gasifier for solar applications. Powder Technology 390 (2021) 482–495. https://doi.org/10.1016/j.powtec.2021.05.032.

IV. M. Suarez-Almeida, A. Gómez-Barea. On the comprehension of the gas split in loop seal devices. *Submitted for publication*

V. M. Suárez-Almeida, A. Gómez-Barea, J. Salinero. Design and performance analysis of a solar dual fluidized bed gasifier. *Submitted for publication*

Montserrat Suárez Almeida is the main researcher for Papers II-V. She performed the model and analysis of Papers II, III and V, part of the modelling work in Paper I and, she planned and executed the experimental work, data evaluation and modelling of Paper IV. She wrote and edited Papers II-V and contributed to the editing work in Paper I. Professor Alberto Gómez Barea is the main author of Paper I and the supervisor of this work, contributing to modelling and experimental work with ideas, discussions and guidance and with the editing and revision of all the publications. Professor Ahmed F. Ghoniem contributed with discussions and editing of Papers I and II. Professor Christoph Pfeifer contributed with discussions and providing the experimental data in Paper III and with editing of Papers II and III. Professor Bo Leckner contributed with discussion, revision and editing of Paper III. Dr. Jesús Salinero contributed with editing of Paper V.

The result of this thesis was submitted to intellectual property,

> M. Suárez-Almeida, A. Gómez-Barea. Módulo de lecho fluidizado dual para gasificación de biomasa y residuos con energía solar e instalación y método de operación asociado, ES1650.153

Additional publications related to the work are listed below but have not been appended as their scope is out of the thesis.

VI. S. Nilsson, A. Gómez-Barea, I. Pardo-Arias, M. Suárez-Almeida, V. F. de Almeida. Comparison of Six Different Biomass Residues in a Pilot-Scale Fluidized Bed Gasifier. Energy Fuels 33 (2019) 10978−10988. https://doi.org/10.1021/acs.energyfuels.9b01513.

VII. M. Suárez-Almeida, A. Gómez-Barea, A.F. Ghoniem, S. Nilsson, B. Leckner. Modeling the transient response of a fluidized-bed biomass gasifier. Fuel 274 (2020) 117226. https://doi.org/10.1016/j.fuel.2020.117226.

The following papers published in proceedings of international conferences overlap with the content in papers I, IV and VII.

VIII. M. Suárez-Almeida, J. Salinero, A.F. Ghoniem, B. Leckner, A. Gómez-Barea. Simulation of the Transient Response of a Fluidized Bed Gasifier for Hybridized Concentrated Solar

Thermal Power Plant. Proceedings of the 23rd International Conference on Fluidized Bed Conversion, Seoul (2018)

IX. A. Gómez-Barea, M. Suárez-Almeida, M. Silva, C. Pfeifer, J. Karl, A. Ghoniem. Hybridization of biomass steam gasification in dual fluidized bed reactor with concentrated solar energy. Proceedings of the International Conference on Polygeneration Strategies, Vienna (2019)

X. M. Suárez-Almeida, A. Gómez-Barea. Fluid-dynamics of a loop seal: an experimental study. Proceedings of the 24th International Conference on Fluidized Bed Conversion, Gothenburg (2022)

Nomenclature

A	cross section, m^2
a	decay coefficient, m^{-1}
A_{wall}	surface area (of the pipe), m^2
C	constant for calculating the decay coefficient *a*, -
c_p	specific heat of solid inert material, kJ kg^{-1} K^{-1}
$d_{gasifier}$	diameter of the gasifier, m
d_p	particle size, m
$E(t)$	residence time distribution, s^{-1}
E_∞	elutriation constant, kg m^{-2} s^{-1}
ER_{H_2O}	steam equivalence ratio, -
F	mass flowrate, kg s^{-1}
F_{char}	flowrate of char leaving the gasifier, kg s^{-1}
F_{inert}	total flowrate of inert material leaving the gasifier, kg s^{-1}
F_s	flowrate of solids inert material, kg s^{-1}
g	gravitational acceleration, m s^{-2}
G_s	solids flux of inert material referred to the riser (to the SC in Chapter 4 figures), kg $m^{-2}s^{-1}$
h	height, m
H_G	specific heat requiered by the gasifier, kJ $kg_{bio,daf}^{-1}$
L	lenght of the pipe, m
n_i	molar yield of species *i* in the product gas (per mol of biomass), -
P_i	pressure at tap *i*, according to Fig. 3.1 (a) or Fig. 4.1, Pa
Q	gas flowrate, m^3 s^{-1}
$R_{C\text{-}H_2O}$	reactivity of char steam gasification, s^{-1}
R_{RC}	fraction of gas flowing through the RC to total gas fed to the loop seal, -
T	temperature, ºC
t	time, s
Th	biomass throughput (referred to the gasifier), kg h^{-1} m^{-2}
u_0	superficial gas velocity, m/s
u_{critic}	critic velocity defined as in Eq. (3.24), m s^{-1}
u_g	actual gas velocity, m/s
u_{mf}	minimum fluidization velocity, m s^{-1}
u_s	solids velocity, m s^{-1}
u_t	particle terminal velocity, m s^{-1}
W	solids inventory, kg
X_{char}	average char conversion in the gasifier, -
x_{O2}	molar fraction of O_2 in the riser fluidizing gas, -

Greek symbols

α	angle of inclination of the pipe in Fig. 3.1, º
β	gas-particle friction coefficient, kg m^{-3} s^{-1}
δ	bubble fraction, -
ΔP	pressure drop, Pa
ε	voidage, -
λ	solid-wall friction coefficient, s m^{-1}
λ_{H2O}	steam to biomass molar ratio, -
λ_{O2}	oxygen to biomass molar ratio, -
μ_g	viscosity of the gas, kg m^{-1} s^{-1}
ξ	constant dependent on the cyclone geometry -
ρ	density, kg m^{-3}
$\rho_{h=0}$	solids concentration at the top of the riser dense zone, kg m^{-3}
σ	referred to the gasifier geometry in Fig. 3.1(a), °
τ_{bio}	biomass space time, s
τ_{char}	average char residence time in the gasifier, s
τ_r	characteristic time of reaction, s
Φ	particle sphericity, -

Subscripts

1	referred to riser primary gas injection
2	referred to riser secondary gas injection
bb	bottom bed
bio	biomass
C	referred to the flowrate of solids coming from the combustor/combustor temperature
daf	dry basis ash free
g	referred to the gas
G	referred to the gasifier
mf	minimum fluidization
p	referred to the particle
s	solids
t	referred to total gas fed to the riser
T	referred to total inventory of inert solids
top	referred to the top of the riser

Abbreviations

1D	one-dimensional
2D	two-dimensional
3D	three-dimensional
BFB	bubbling fluidized bed
bio	biomass
C1	referred to configuration 1 (according to Fig. 2.2)

C2	referred to configuration 2 (according to Fig. 2.2)
C3	referred to configuration 3 (according to Fig. 2.2)
C4	referred to configuration 4 (according to Fig. 2.2)
CFB	circulating fluidized bed
CFD	computational fluid dynamics
CFM	cold flow model
DC	down comer
DFB	dual fluidized bed
DFBG	dual fluidized bed gasifier/gasification
DNI	direct normal irradiance
EM	equilibrium model
FB	fluidized bed
FBG	fluidized bed gasifier
HHV	high heating value
HMS	hot material storage
KM	kinetic model
LHV	low heating value
LLS	lower loop seal
PEM	pseudo-equilibrium model
RC	recycle chamber
SC	supply chamber
SDFBG	solar dual fluidized bed gasifier
SEH	specific external (solar) heat
TDH	total disengagement height
TES	thermal energy storage
TU-Wien	Vienna University of Technology
ULS	upper loop seal
WGSR	water-gas-shift reaction
WMS	warm material storage

Provando e riprovando…

Chapter 1. Introduction

In recent years, limited availability of fossil fuels and concerns over energy-supply security, together with the need to reduce greenhouse gas emissions have placed the development of renewable fuels in the spotlight. Steam gasification of biomass and wastes appears as an attractive process producing high-quality syngas (N_2-free, with high concentration of H_2 and low concentration of CO_2) which can be further processed in catalytic reactors to produce renewable fuels and/or chemicals.

Steam gasification of biomass is an endothermal process, requiring significant heat at high temperature (750-1000 ºC) to drive the reactions. Autothermal gasification in which part of the fuel is burnt to generate the necessary heat to maintain the process is the most developed technology at industrial scale. Two approaches can be followed for producing N_2-free syngas from autothermal gasification: the use of pure oxygen as oxidizing agent, requiring from an air separation unit, which is energy-intensive and costly or, the use of air in a dual fluidized bed gasifier (DFBG), trading the cost and energy penalty of an air separation unit for a more complex gasification system. Allothermal gasification, using heat from an external source to drive the process, appears as a more interesting process for maximizing the gasification efficiency and at the time producing a high quality syngas with high share of hydrogen.

In allothermal gasification the external heat source would ideally make it possible to transfer all the energy available in the fuel into the produced syngas, instead of burning some to provide the heat, hence significantly raising the syngas yield and improving the overall energy efficiency of the process. In turn, steam gasification transforms heat into chemical energy in the syngas with higher exergy and thus acts as a chemical heat pump. On the other hand, allothermal gasification can be seen as a method of water reduction (splitting) using the carbon in the fuel as reducing agent, generating additional hydrogen from water during the fuel reforming (so H_2 comes from water and fuel).

The use of solar energy as external heat source for steam reforming of fuels has been recognized as a highly attractive option [1], generating solar biofuels with maximum share of renewable energy in storable form. Given that the biomass availability and relatively high cost entail limitations in the scale and location of the plant [2], solar biomass hybridization appears as an attractive technology for improving operational flexibility.

Solar gasifiers can be classified according to (i) the type of gas-solid contact, roughly as packed bed, fluidized bed, and entrained flow gasifiers, or (ii) the way in which solar radiation contacts the reactants, basically as directly-irradiated, where the solid carbonaceous reactants are directly exposed to radiation, and indirectly-irradiated, where the radiation strikes an intermediate material such as an opaque wall or energy carrier, which in turn irradiates the reacting chamber.

Regarding the gas-solid contact, fluidized-bed reactors are considered the solar gasifier with highest scaling-up potential since they overcome the strict particle size needs of entrained-flow

reactors and, the transport limitations of packed-bed gasifiers due to the higher rates of mass and heat transfer.

Respecting the solar radiation contact, direct irradiation offers superior heat transfer characteristics and energy efficiency, but the reactor must have a transparent window, which can be fouled by operation. A particular effort has been made to develop directly-heated solar fluidized bed gasifier (FBG) and many devices have been tested at lab-scale in transparent devices for the gasification of carbonaceous fuels [3–6]. Indirect irradiation, in which an intermediate medium is heated by solar radiation and transported to the gasifier, has less favorable heat transfer attributes but avoids the difficulties with direct irradiation design [7]. Three approaches have been proposed to indirectly supply the concentrated solar radiation to the reactor: (i) irradiating the reactor external sidewalls [8]; (ii) using a two-cavity reactor [9]; and (iii) using a heat carrier [10–13]. A wide discussion on the development reached by different solar gasifiers is presented in **Paper I** while further information can be found elsewhere [14,15].

Indirect solar gasification using a heat carrier is the only approach which allows to decouple the operation of the gasifier from the intermittency of the solar radiation by an intermediate thermal energy storage (TES). The first attempt on addressing the issue of solar energy intermittency to warrant the continuous operation of the gasifier was proposed very early [16] by the use of two heat carriers: solar-heated molten slags were stored, while steam was used to drive the heat from the thermal storage to the gasifier. Subsequently, similar concepts have emerged but simplified by the use of a single heat transfer medium: molten salt where proposed in [12] for supercritical water gasification while solids particles where proposed for conventional gasification [7,10,11] since they allow higher operating temperatures.

The use of solid particles as an energy carrier is attractive since they are an excellent thermal energy storage medium, operating at high temperature and low cost. Solid particles were proposed as heat transfer and thermal storage medium in the early 1980s [17,18] because of their ability to withstand high temperatures and the straightforward integration of solar energy collection and TES, but the technology faded soon after. Only in recent years, driven by the need of achieving higher temperatures together with cheap TES, solid particle technology has been the subject of new research interest [19]. The current technology of particle solar receiver reaches temperatures of 1000 °C [19,20] allowing the hybridization of solar energy with processes requiring energy at high temperature such as biomass gasification. A brief discussion on the key issues of solid particle solar receivers is provided in **Paper I**.

1.1. Motivation, aim and scope

This thesis is motivated by the lack of a technology for the implementation at scale of allothermal steam gasification. Despite the fact that a great number of allothermal steam gasifiers have been developed at laboratory or bench scale, none has been scaled up or commercialized due to practical problems derived from the difficulty of producing a steady syngas in spite of solar radiation variation, as well as the implementation of heat transfer at large scale. Therefore, steam gasification has only been conducted at scale using indirect air-steam dual fluidized bed gasifiers (DFBG). This technology produces a high quality syngas (N_2-free and high H_2 content), while the gasifier is thermally supported by the sensible heat of circulating solid material coming from a separated air-combustion unit. Fuel for combustion comes either from the fuel fed to the gasifier (unconverted char) which is circulated to the combustor, or from additional fuel directly fed to the combustor. As a result, the gasification unit is allothermal, since the heat comes from a separated unit, but the system as a whole is autothermal (when there is no direct addition of fuel to the combustor).

The aim of this thesis is to extend the possibilities of the classical air-steam DFBG following the approach in [10,11], by considering that the system can be thermally supported by external heat. The most attractive case implies that all the energy supply to the gasifier is renewable i.e., biomass

as solid fuel and solar energy as external heat. Under an ideal operation solar energy completely meets the heat demand of the gasification process and all carbon from the biomass is converted to fuel volatiles, resulting in a syngas embodying (in the form of sensible and chemical energy) not only all the energy from the biomass but also an additional share of solar energy.

The scope of this thesis is to assess the hybridization of biomass gasification in dual fluidized bed (DFB) with concentrated energy from a solar tower using solids particles as heat carriers. The process is to be analyzed from the chemical reactor engineering perspective, coming up with an optimal reactor design that allows a continuous operation of the gasifier independent of the intermittency of the solar resource. The thermal integration between the DFBG and the solar field is considered to optimize the reactor design and operation. However, the solar energy is directly considered as an input parameter since, the performance analysis of the of the solar receiver and solar field by modelling is out of the scope of this work.

1.2. Methodology

Modelling is the main tool used in this work for understanding both, the thermochemical performance of biomass steam gasification and the fluid-dynamics behavior of DFBGs, and to design the new SDFBG. A previously developed pseudo-equilibrium model (PEM) was used to assess the steam gasification of biomass while, semi-empirical models were used for the fluid-dynamics analysis. Moreover, experimental data from a DFBG cold flow model (CFM) were compared against the results of the DFBG hydrodynamic model developed.

This work experimentally addresses the existing knowledge gap related to the operation of loop seals as non-mechanical valve, as these devices have a key role in DFB units. Dedicated experimental measurements, mainly based on pressure and solids height samplings, were carried out in an isolated loop seal CFM to shed light on the understanding of the fluid-dynamics of these devices.

1.3. Outline of the thesis

This thesis comprises an extended summary based on the five papers appended. Fig. 1.1 gives an overview over the structure of the thesis whose final aim, presented in detail Chapter 5, is the design of a dual fluidized bed reactor for carrying out solar steam gasification. Previous to the design, solar steam gasification process and its thermal integration with the solar field and energy storage along the year was assessed in Chapter 2, and fluid-dynamics issues in Chapters 3 (complete DFB loop) and 4 (loop seal). The contents of the appended papers are briefly summarized below.

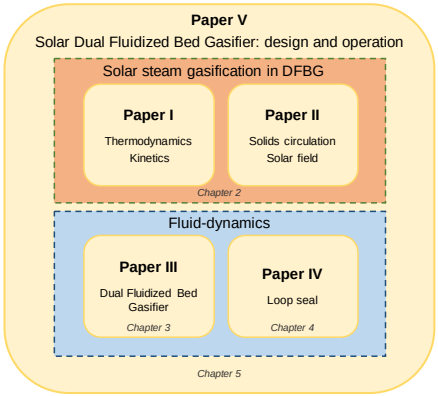

Fig. 1.1. Outline of the thesis.

Paper I reviews the state of the art of the most important features for developing the proposed SDFBG, analyses the thermodynamic and kinetic aspects of allothermal gasification. The char conversion and the performance of a conventional (non-solar) DFBG are assessed by modelling to assess the potential of a DFBG to be retrofit into SFBG. The results from these preliminary analysis delimits the window of the operating conditions and demonstrated the potential of the SDFBG. A first theoretical analysis of the reactor performance of the SDFBG is provided.

Paper II applies the knowledge gained in Paper I for the analysis of the performance of the DFBG integrated with the solar side. The circulation of solids (internal and external) and the allowable solar heat supply to the system are compared for different integrations of the external solids circulation into the DFBG; two of them were identified as the most advantageous for implementation in the process. The separation and storage of char is identified as a method to provide the system with significant flexibility. Moreover, the operation under daily and seasonal weather variations throughout the year is studied by the developed model, coupled to a solar field using hourly data from a specific location.

Paper III focuses on modelling the fluid-dynamics of a DFBG. The DFBG CFM at TU-Wien was used as reference unit and, the results of the model were compared with measurements. The model was used to theoretically assess the performance of conventional DFBGs and to preliminary assess the fluid-dynamic limitations of SDFBGs. The model was also used to analyze the performance of loop seals in DFB systems, which resulted to be very advantageous devices for the development of the proposed SDFBG.

Paper IV presents the experimental study carried out in an isolated loop seal CFM. The study was intended to shed light on the existing controversies related with the fluid-dynamics performance and modelling of loop seals, looking for optimizing its design and operation within the proposed SDFBG. It was found that the fluid-dynamics behavior of loop seal devices is governed by non-ideal gas-solids flow patterns that cannot be addressed by simple semi-empirical 1D models.

Paper V gathers all the knowledge gained from paper I-IV for the design of a flexible SDFBG able to operate both under autothermal and at highly allothermal conditions. The previously identified most advantageous integration options of the external solids circulation into the DFBG were considered, leading to different design and operation requirements. The performance of the SDFBG is analyzed under a wide range of solar external heat loads, and the flexibility of the unit, under different operating condition, is assessed by sensitivity analysis.

Chapter 2. Solar steam gasification in DFBG

2.1. Process layout

The proposed system is thought to combine the current technology of the DFBGs with the solar side. The conceptual integration of the solar gasification system and particle receiver is presented in Fig. 2.1. Solid particles act as thermal energy carrier, circulating between the solar receiver and the gasifier. Two tanks allow for temporary thermal storage of solar energy: the hot material storage (HMS), to store the particles heated in the solar receiver, and the warm material storage (WMS), to store the particles leaving the gasification system. In Fig. 2.1, the DFB gasification system is represented inside the dash-dotted line, it is composed of: a bubbling fluidized bed (BFB) gasifier, where the biomass is injected, devolatilized and the char is partially gasified with steam, and a fast fluidized bed combustor, where the char coming from the gasifier is burned with air. In this arrangement, the gasifier is heated by both the circulating hot material coming from the combustor and that coming from the HMS.

The reactor in Fig. 2.1 will operate with high share of external heat during the summer-light hours or when there is TES available, while it will send more char to the combustor (and thus generating more heat from char oxidation) when the fraction of solar external heat decreases (at nights or during winter time). When the system operates only supported by external solar energy (i.e. without burning char in the combustor) it will provide the highest solar share in the syngas (defined as the fraction of chemical energy in the product gas coming from the solar energy), converting the whole fuel into product gas. However, converting all the char in the gasifier would require a significant char residence time and, although some studies have been done on this [21], a gasifier design for that purpose is yet to be reported.

Separation of the char from the solids leaving the gasifier during periods of high solar irradiance is an interesting option to increase the solar share in the system, which entails no special requirements in the gasifier design. Under this mode, the system operates allothermically (avoiding char combustion) when solar energy is available, while the separated char is stored for reintroducing it into the system in periods of low/absence of solar irradiance. A wide discussion on the implications of this option in the process is presented in **Paper II**. Although the mixture of bed material and char can theoretically be separated using a fluidized bed (due to the significant difference in the density and size of particles) the available knowledge on this topic is limited [22,23]. Therefore, this thesis is focused on maximizing the solar share while increasing the char conversion in the gasifier. Further research to assess the real effectiveness of char separation in a system like the one proposed is an interesting extension.

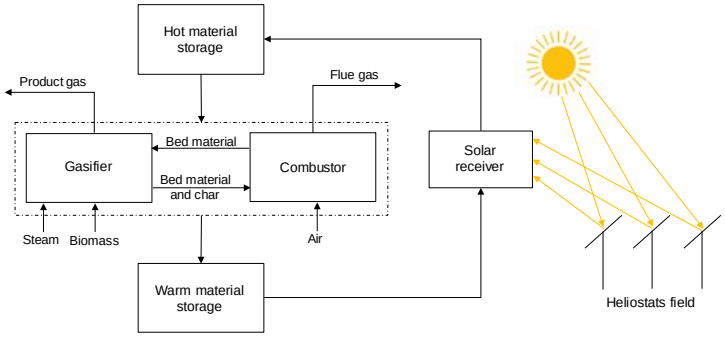

Fig. 2.1. Solar hybridized dual fluidized bed concept.

In a standard (non-solar) DFBG, there is only internal solids circulation between the units (as shown in the system inside the dash-dot-lined box in Fig. 2.1) while in the SDFBG there is also external solids circulation (through the solar loop). Furthermore, there are different alternatives for the integration of this external solids circulation into the system, as shown in Fig. 2.2. As a result, depending on the integration, the solids circulation from the gasifier to the combustor can substantially differ from that of the combustor to the gasifier. The selection of the optimal configuration is a matter of concern since the biomass space time (τ_{bio}, see Section 2.2.4) is different depending on the configuration. In addition, the presence of active (biomass, char and ash) particles in the solar receiver may present technical limitations in some solar particle receivers [19]. The presence of active material in the solar loop is avoided/minimized in C2 and C4 since the particle stream is removed from the combustor, where the char concentration is the lowest in the system.

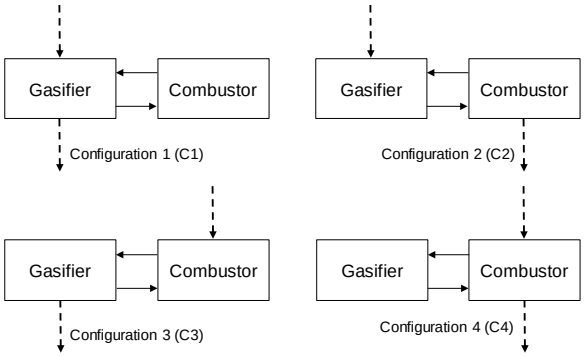

Fig. 2.2. Configurations for the direct integration of the solids heat carrier in the SDFBG system (- - - circulation from/to the solar loop).

2.2. Modelling

2.2.1. Biomass steam gasification modelling approach

The complete conversion of 1 mol of wood biomass with general formula $CH_{1.5}O_{0.7}$ [24] by steam gasification to yield syngas (H_2 and CO) and hydrogen (and CO_2) can be represented by reactions R1 and R2, respectively.

$$CH_{1.5}O_{0.7} + 0.3H_2O \rightarrow 1.05H_2 + CO \quad \text{(R1)}$$

$$CH_{1.5}O_{0.7} + 1.3H_2O \rightarrow 2.05H_2 + CO_2 \quad \text{(R2)}$$

Gasification is an endothermal process requiring significant heat to drive the reactions. The standard heat of reaction at 25 ºC of R1 and R2, considering a biomass high heating value (HHV) of 20 MJ/kg, is, respectively, 75.6 kJ/mol (3.06 MJ/kg) and 34.5 kJ/mol (1.40 MJ/kg). However, this is just an ideal reference case and not the actual situation of biomass gasification in FBG which, due to thermodynamic and kinetic limitations must be conducted at high temperature (750–1000 °C) and results in a more complex product distribution [25] as indicated in R3.

$$CH_{1.5}O_{0.7} + \lambda_{H_2O} H_2O \rightarrow n_{H_2} H_2 + n_{CO} CO + n_{CO_2} CO_2 + n_{CH_4} CH_4 + n_{C_2H_4} C_2H_4 + n_{H_2O} H_2O + n_{C_{10}H_8} C_{10}H_8 + n_{C_{(s)}} C_{(s)} \quad (R3)$$

Besides CO and H_2, the product gas contains: hydrocarbons, CH_4 and other light compounds and tars, unconverted char and unconverted steam (even when feeding the stoichiometric steam according to R1). Calculating the distribution of syngas and char for different operating conditions in a FBG is complex and different models are employed. Three approaches can be applied to model steam gasification in an FBG [26]: (i) equilibrium model (EM); (ii) kinetic models (KM), taking into account chemical and fluid-dynamic rate consideration and, (iii) the combined approach, sometimes called pseudo-equilibrium (PEM). EM is the most universal way to close the calculations but fails in predicting real gas composition and fuel utilization (char conversion). KM gives better representation of the process for a specified system (geometry, type of biomass, etc.) but a great deal of inputs is required, and the conclusions are system-dependent. PEM is based on equilibrium relations together with semi-empirical inputs to take into account kinetic and flow rate limitations. It is a reasonable compromise between EM and KM using some comprehensive models supported by empirical closures. Although the steam gasification process in this thesis is always modelled following the PEM approach, the EM is analyzed in **Paper I** to thermodynamically quantify the ideal process and, to understand the effect of kinetic limitations (a summary is given in Section 2.3.1).

2.2.2. Model of the solar DFBG

The model of the SDFBG comprises the gasification and combustion units and considers the solids stream coming from the solar loop.

The steam gasification process (in the gasifier unit) is represented by R3 where for the sake of simplicity moisture and ash free biomass is considered, the char is assumed to be pure solid carbon $C_{(s)}$ and, the light hydrocarbons are lumped into ethylene (C_2H_4) and tars into naphthalene ($C_{10}H_8$).

The gasifier is modelled following the approach described in [25]. The process is simplified by decoupling primary and secondary conversion in two sequential imaginary zones, a devolatilization zone and a reduction zone as sketched in Fig. 2.3. The primary yields of devolatilization are converted in the reduction zone, as represented by the dashed line in Fig. 2.3. The char is gasified, methane is reformed with steam, ethylene is dehydrogenated and the tar converted by reforming/cracking. The composition of the outlet gas is obtained by applying the equilibrium of the water-gas-shift reaction (WGSR) to the compounds released after devolatilization (i.e., fed biomass except unconverted C_2H_4, CH_4, tar and char), and considering the overall atomic mass and heat balance over the entire gasifier while taking into account the unconverted fraction of hydrocarbons, tar and char.

Other assumptions for modelling the gasification reactor are: (i) conversion of gaseous species assuming perfect mixing of gases both, in the bed and freeboard, and first order kinetics, with average gas residence time of 1 s (the actual geometry of the reactor is not considered); (ii) char is removed from the gasifier with the solids circulating to the combustor and/or to the solar loop (neither elutriation nor mechanical removal of bottom ash are considered) and (iii) the char is converted by steam gasification considering that the particles are perfectly mixed in the reactor and following the uniform conversion model (further details are given in Section 2.2.3).

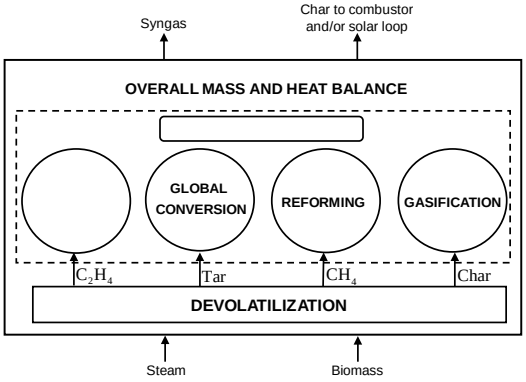

Fig. 2.3. Scheme of the steam gasification model adopted in this work. The reactions indicated are global to qualitative give and overall description of the main conversion processes.

If the gasification temperature, steam to biomass fed (λ_{H2O}) and inlet temperature of the gasification agent are specified, there are 9 unknowns (heat necessary for gasification, H_G, and the 8 yields of species in the product gas, n_i). The problem is solved considering the 4 balance equations (three atomic balance equations, CHO, and one heat balance) and 5 additional equations (conversion of CH_4, C_2H_4 and tar according to kinetics rates, equilibrium of WGSR and char conversion sub-model).

The combustion unit has been modelled assuming instantaneous and complete conversion of the char coming from the gasifier and char storage, i.e. no unburnt char enters the gasifier with the solids coming from the combustor [27]. The overall process in the combustor is given by,

$$C_{(s)} + \lambda_{O_2} O_2 + 3.76\,\lambda_{O_2} N_2 \rightarrow CO_2 + 3.76\,\lambda_{O_2} N_2 + (\lambda_{O_2} - 1) O_2 \qquad \text{(R4)}$$

The heat necessary for gasification (H_G) comes from the solids circulating from the combustor ($F_{s,C}$) and HMS ($F_{s,HMS}$). Eq. (2.1) is the coupling equation for configurations C1 and C2 (Fig. 2.2), in which the solids from the HMS are introduced into the gasifier, and Eq. (2.2) for C3 and C4, in which the solids from the HMS are introduced into the combustor so that all the solids into the gasifier come from the combustor. Note that, for the sake of simplicity, the sensible heat of active particle, i.e., char, which represents a small fraction of the stream (< 3%), is neglected.

$$H_G = F_{s,C}\, c_p (T_C - T_G) + F_{s,HMS}\, c_p (T_{HMS} - T_G) \qquad (2.1)$$

$$H_G = F_{s,C+HMS}\, c_p (T_C - T_G) \qquad (2.2)$$

When modelling the char conversion in system under C1 and C2, the concentration of char in the solids stream from the HMS is assumed to be equal to that of the gasifier (in agreement with the assumption of perfect mixing of solids). For a given solar external energy supplied to the system the model estimates the char to be burnt in the combustor to balance the heat requirements in the gasifier, as well as the corresponding average residence time of the char particles in the gasifier (τ_{char}) to completely convert the remaining char in the gasifier (that, which is neither circulated to the combustor nor stored).

When analizing the performance of the system joined to the solar field, the transient response of the SDFBG is considered faster than the hourly irradiance variations (hourly pseudo-stationary model). This asumption must be treated with caution since there are operating conditions where the rate of change of the process can be of the same order of magnitude. The solar field, considering Sevilla as location of reference, was sized for a solar multiple (defined as the ratio between the area

of heliostat field and that require to meet the heat demand of the gasifier at the peak solar thermal output) of 2.5 and a SDFBG operating at a maximum char conversion of 78%. A TES of 19.8 MJ/$F_{bio,daf}$ was selected for the analysis as that allowing to run the gasifier at maximum char conversion, during 24 h/day for the reference case in summer (Fig. 2.8(c)).

A summary of the operating conditions set for the base case study is given in Table 1 and some of them are discussed in Section 2.3.2. More details of the model as well as other required input data (devolatilization yields, kinetic expressions, etc.) are reported in **Paper II**.

Table 2.1. Summary of the operating conditions set for the base case study of the SDFBG (it is specifically detailed when variations of these parameters are considered in the analysis).

Gasifier temperature, T_G	ºC	850
Combustor temperature, T_C	ºC	905
HMS temperature, T_{HMS}	ºC	950
Steam temperature	ºC	750[1]
Air temperature	ºC	25
Steam equivalence ratio, ER_{H_2O}[2]		2 [28]
Air fed over the stoichiometric in the combustor	%	20
Pressure of operation	Pa	101 325

[1] Considered as the maximum achievable after the energetic integration of the system
[2] Steam fed into the gasifier over that required to stoichiometrically convert the biomass into syngas (H_2 and CO)

2.2.2.1. Char conversion

The conversion of the char is the rate-controlling process in FBGs where, in general, it is difficult to fully convert the solid carbon. Even in units operating with high temperature and reactor volumes, or when an external catalyst is used, the backmixing of solid particles makes complete char conversion difficult in one single bed. The extent of char conversion in the gasifier depends on the carbon-steam gasification rate of the char particles (CO_2-carbon rate is slower) and their residence time in it. On the one hand, the rate of reaction depends on the temperature, the species concentration (mainly steam, but hydrogen can be also important as it inhibits the carbon-steam reaction rate), the intrinsic reactivity of the char (fuel type and form of char generation), and the quality/extent of gas-solid contact. On the other hand, the residence time of the char particles depends on the rate of solids removal that can be unintentionally happen by gas-solid elutriation from the bed and/or, in the case of DFBG, by removing the solids to carry them to the combustor. Theoretically, in a FBG without any kind of char removal the residence time of char could be infinite, and consequently, the char conversion could be complete. In practice, due to kinetic limitations, there is a throughput of char flow rate (i.e., kg m^{-2} s^{-1}) that can be converted in a gasifier with a given solid inventory.

The char conversion in the gasification unit of a DFBG depends on the heat balance of the system: while in a conventional autothermal DFBG, the char conversion is very limited since a significant fraction is burnt in the combustor to thermally maintain the system; in a SDFBG, the fraction of char burnt in the combustor is reduced, and that converted in the gasifier increased, as more external solar heat is provided. Moreover, the char conversion and residence time in the gasifier are directly linked to the gasifier solids inventory and solids circulations. Therefore, the conversion of char in the gasifier is a key step in modelling the performance of both solar and standard DFBGs.

The char conversion model applied in this work is summarized by Eqs. (2.3-6). The uniform conversion model with kinetic control was adopted for representing the single particle conversion which, after integration results in Eq. (2.4) . The average char conversion in the gasifier is calculated according to Eq. (2.3) by considering a population balance of perfectly mixed char particles (i.e., according to the residence time distribution given by Eq. (2.5)) and perfect mixing of gas. Integrating Eq. (2.3) leads to Eq. (2.6), where the char conversion is just function of the characteristic time of

reaction, τ_r, estimated from the reaction rate of the char steam gasification as in Eq. (2.7) and the average residence time of char particles in the gasifier, τ_{char}, defined as in Eq. (2.10).

$$X_{char} = \int_0^\infty x_{char}(t)\, E(t)\, dt \tag{2.3}$$

$$x_{char}(t) = 1 - \exp(-t/\tau_r) \tag{2.4}$$

$$E(t) = \frac{1}{\tau_{char}} e^{t/\tau_{char}} \tag{2.5}$$

$$X_{char} = \frac{\tau_{char}/\tau_r}{1 + \tau_{char}/\tau_r} \tag{2.6}$$

$$\tau_r = \frac{1}{R_{C-H_2O}} \tag{2.7}$$

where, is the instantaneous reactivity of a single char particle which for the UM only depends on temperature and gas reactant composition (c_i),

$$R_{C-H_2O}(T, c_i) = \frac{1}{x_{char}} \frac{dx_{char}}{dt} \tag{2.8}$$

2.2.3. Performance indicators

The following parameters are defined to assess the results of the model.

Biomass space time (τ_{bio}) defined as the ratio between the mass inventory of the gasification unit and the mass flowrate of biomass

$$\tau_{bio} = \frac{W_{bed}}{F_{bio}} \simeq \frac{W_{inert}}{F_{bio}} \tag{2.9}$$

where the approximation takes into account that the bed is mainly composed by inert material (sand, olivine, etc.) and the char holdup in the reactor is much less significant for practical operating conditions.

Average residence time of the char particles in the gasifier defined as the ratio of char holdup and flowrate of char leaving the gasification unit, i.e.,

$$\tau_{char} = \frac{W_{char}}{F_{char}} \tag{2.10}$$

Assuming perfect mixing of solids in the gasifier (a reasonable hypothesis in a low-velocity operated BFB), the stream of solids leaving the gasifier has the same composition as that inside the gasifier so it holds,

$$\frac{W_{inert}}{W_{char}} = \frac{F_{inert}}{F_{char}} \tag{2.11}$$

F_{inert} being the flowrate of inert material leaving the gasifier. By combining Eqs. (2.9-11) the biomass space time can also be expressed as:

$$\tau_{bio} = \tau_{char} \frac{F_{inert}}{F_{bio}} \quad (2.12)$$

Specific external heat supplied to the system (SEH) defined as the amount of heat coming from the solar field/HMS that is introduced per kilogram of dry-ash-free biomass (daf).

Solar share defined as the ratio between the SEH and the lower heating value (LHV) of the syngas (expressed in percentage). This is sometimes called solar-into-chemical efficiency, referring to the fraction of chemical energy coming from the solar energy, embodied in the product gas. Sometimes the solar share is defined in relation with the energy in the biomass i.e., SEH/LHV_{daf} giving values higher than the one defined in this works. The latter definition is most usually called fuel upgrading. In this work the first definition is used for all the calculations.

Cold gas efficiency, defined as the ratio between the chemical energy in the syngas and that in the biomass, expressed in percentage (the chemical energy is calculated by lower heating value for both biomass and syngas).

2.3. Summary of main results

2.3.1. Allothermal steam gasification

The equilibrium predictions in Fig. 2.4 (a) show that, at low temperatures, solid carbon ($C_{(s)}$) and CH_4 are present in the product gas, but both disappear by reforming as the temperature is increased. The carbon boundary point (temperature at which the solid carbon is fully converted) is about 1200 K for ER_{H_2O}=1, decreasing with ER_{H_2O} (for instance, although not shown in the figure, it is about 900 K for ER_{H_2O}=4.33). CH_4 virtually disappears at 1200 K and the CO and H_2 increase with temperature as they are the main products of carbon and methane reforming. The increase is very significant as long as there is solid carbon in the system whereas the increase slows down once the solid carbon is reformed. For ER_{H_2O}=1 and T>1200 K, the syngas is practically H_2 and CO as given by the stoichiometry of reaction R1.

The corresponding heat required for gasification (the heat of reaction R3 assuming the equilibrium is achieved) as a function of temperature is presented in Fig. 2.4(b) for various fuels. It is shown that the heat for gasification increases with temperature up to 1200 K (923 °C) for practically all the fuels, i.e., up to the point where the fuel is practically converted into CO and H_2 as shown in Fig. 2.4(a). For biomass with LHV of approximately 18–18.5 $MJ/kg_{bio,daf}$ at around 1000–1200 K (727–927 °C), the heat of gasification ranges between 3.5 and 5.5 $MJ/kg_{bio,daf}$ (80–130 $kJ/mol_{bio,daf}$). The higher the carbon to hydrogen ratio of the fuel, the larger the heat necessary and the more water is split as observed in the figure where the region of biomass (green) is well below that for char from wood (blue) and pure carbon (black). However, on the basis of the heating value of the fuel, the ratio to be supplied to the gasifier ($MJ/kg_{fuel,daf}$) is of the same order for all fuels (25–35% of the LHV of the fuel).

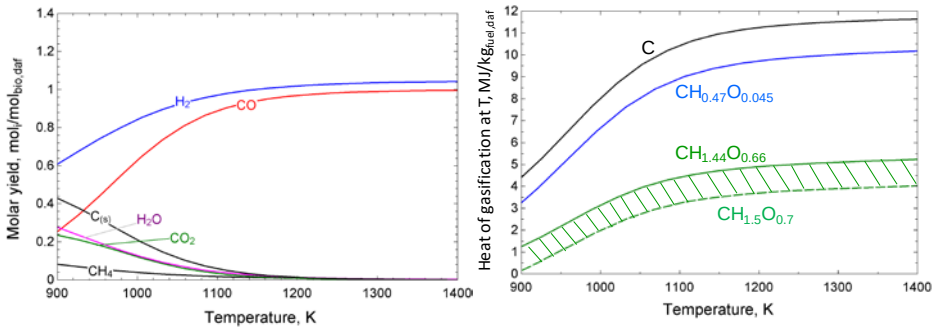

Fig. 2.4. Effect of temperature in allothermal steam gasification on (a) molar gas yields of the main species for steam gasification of biomass according to R1 (tars and other light hydrocarbons are not depicted as their concentrations are very low compared to the rest of species) and (b) specific heat of steam gasification at temperature T according to R1 (per kg of dry-and-ash-free fuel) for different fuels: carbon, char, and biomass (the hatched region in the figure corresponds to a typical biomass). Equilibrium predictions, $ER_{H_2O} = 1$.

An important issue for the present work is that the heat to be supplied to the gasifier is much higher if the equilibrium is attained, as the reforming of hydrocarbons and the gasification of char (highly endothermic reactions) are almost completed, releasing more H_2 species. According to the results presented in **Paper I** the EM predicts 2–3 times more heat than PEM. This is because as the gasifier is limited by kinetics factors, a great deal of carbon, methane, and hydrocarbons are not reformed and the heat required is much lower. In effect, at 850 °C, for instance, around 0.14 LHV of the energy is necessary in the gasifier according to PEM, whereas about 0.25 LHV is predicted by EM. The conclusion is that the more complete the ideal reaction (R1) to syngas (CO and H_2), the higher the energy is stored in the product gas, which is a key aspect for the design of the solar gasifier.

2.3.2. Setting the operating conditions of the SDFBG

To select the range of operating temperatures of the gasification and combustion units in the solar DFBG system, the char conversion in a stand-alone FBG and, the performance of a conventional (non-solar) DFBG were assessed in **Paper I**.

From the analysis of char conversion by steam gasification in a gasifier (see Fig. 9 in **Paper I** for details), it is concluded that the residence time required by a char particle to achieve half conversion is reduced one order of magnitude (from 10-30 min to 1-3 min) when increasing the temperature from 800 to 900 ºC and, that at 850 ºC, an 80% char conversion can be reached at still reasonable char residence time of 40 min.

Fig. 2.5 shows some results for the operation of a conventional DFBG. It is observed (Fig. 2.5(a)) that the operation at high gasification temperature increases the heat requirement in the gasifier (due to char and tar conversion enhancement [26]), leading to higher solids circulation ratios and char burning in the combustor (i.e., lower char conversion in the gasifier). On the other hand, operation at low gasification temperatures allows maximizing the incoming solar heat per unit of inert solids input (maximum temperature achievable in solids solar receivers under development is around 900–1000 °C [19,20]). Fig. 2.5(b) shows that keeping the solids circulation below 30-40 $kg_{solids}/kg_{bio,daf}$ it is possible to operate the system with a difference of temperature between the gasifier and combustor in the range of 40-50 °C, which are reasonable figures in conventional DFBG [28–32]. Ash sintering above 900 °C is another limiting factor when selecting the temperature in the combustor. As a compromise to meet all the mentioned aspects, a gasification temperature of 850 °C and a combustion temperature of 905 °C are selected for the base case afterwards analyzed. The

temperature of the solids coming from the HMS is set at 950 °C, considering the difference of temperature between the HMS and the extraction point (gasifier or combustor) to avoid too high solids circulation ratios, together with a conservative value according to the limitation of temperature reached in particle solar receiver.

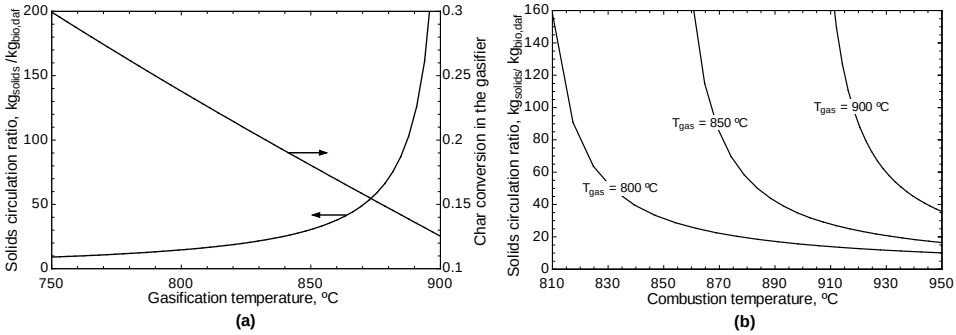

Fig. 2.5. Operation of a conventional (non-solar) DFBG at ER_{H_2O}=2. (a) Solids circulation ratio and char conversion in the gasifier as a function of the gasification temperature for a combustor temperature of 905 ºC; (b) solids circulation ratio as a function of combustor temperature for three gasification temperatures.

2.3.3. Solar DFBG

2.3.3.1. Performance of the SDFBG

Fig. 2.6 shows the performance of an SDFBG for the base case and C1 in Fig. 2.2 as a function of the specific external heat supplied to the system (SEH).The internal solids circulation decreases significantly with SEH as a result of the lower requirement of heat from char combustion, whereas biomass space time increases (Fig. 2.6(a)) since a larger reactor is needed to increase the conversion of char in the gasifier. Clearly, no internal circulation is needed when all the heat required by the gasifier is supplied externally by the solar energy, i.e. allothermal gasification, which is reached at SEH≈3 MJ/kg$_{bio,daf}$. According to Fig. 2.6(b), char conversion of 70–80% can be reached in the gasifier with residence time of 20–30 min (requiring about 2–2.4 MJ/kg$_{bio,daf}$). This can be achieved in a stand-alone low-velocity bubbling FBG but current gasification unit in DFBG, typically operated with char residence time in the range of 1-5 min (10-30% char conversion), would need to be modified to operate at high share of solar heat supply. Higher char conversion than 80% requires excessive long char residence time and thus gasifier volumes. For instance, 90% of char conversion is achieved when the SEH to be supplied is roughly 2.7 MJ/ kg$_{bio,daf}$, requiring to triple the char residence time in the gasifier (about 100 min).

Fig. 2.6(c) shows that the syngas yield and its hydrogen share is increased considerably with SEH as a result of higher steam-char conversion. Fig. 2.6(d) shows that for the maximum SEH (3 MJ/kg$_{bio,daf}$), 15% of solar energy is embodied in the product gas in the form of chemical energy. This results in an increase in the cold gas efficiency from 83.7% in the conventional (non-solar) DFBG operation (SEH=0) to 106.5% for the maximum SEH. Note that, with respect to the autothermal (no-solar) case, in the completely allothermal operation not only the 3 MJ/kg$_{bio,daf}$ from the solar energy are converted into chemical energy in the syngas, but also 1.25 MJ/kg$_{bio,daf}$ which result from the net transfer from sensible to chemical energy. This is explained by comparing the sensible energy leaving the system with the gas streams (fluegas+syngas) in the autothermal and allothermal case: the increase in sensible energy of the syngas leaving the system is 0.13 MJ/kg$_{bio,daf}$, whereas the decrease in the sensible energy of the fluegas is 1.38 MJ/kg$_{bio,daf}$. Being, therefore, demonstrated the high potential of solar thermal energy to increase the chemical energy of a non-solar DFBG.

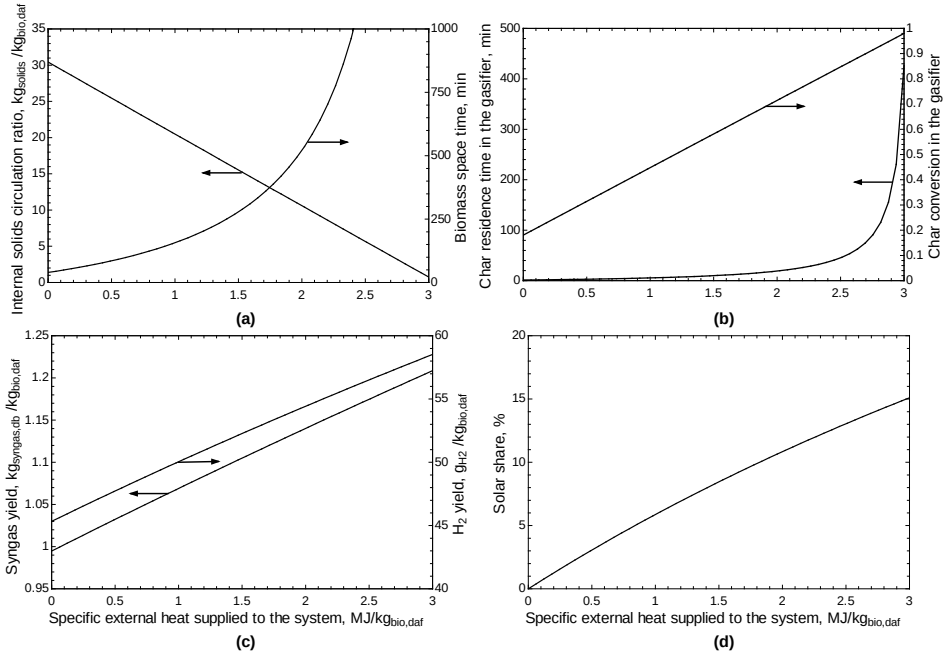

Fig. 2.6. Performance of a SDFBG as a function of external heat supplied to the system (SEH) for C1.

The four configurations presented in Fig. 2.2 have been analyzed to assess the required external and internal solids circulation as a function of the specific external heat SEH (see **Paper II**-Appendix A for details). The results are synthetized in Fig. 2.7 through the analysis of the biomass space time, (an indirect indicator of the solids circulation as shown in Section 2.2.4). It can be seen that, for a given SEH, the biomass space time is higher for C3 and C4 than for C1 and C2. The reason is that in C3 and C4 all the solids reaching the gasifier come from the combustor, requiring higher internal circulation ratio than in C1 and C2, in which the solids from the solar loop, with a higher temperature than that of the combustor, are introduced in the gasifier. It is shown that reaching a char conversion of 78% (SEH = 2.2 MJ/kg$_{bio,daf}$) in the gasifier requires a biomass space time of 1000 min in C3 and C4 (at any combustion temperature), while in C2 and C1 is achieved for a much lower biomass space time (640 min with combustor temperature of 870 °C and 680 min, with combustor temperature of 905 °C, respectively). Note that operating the SDFBG under C2 requires from modifying the temperature of the combustor (by decreasing it) while increasing the SEH.

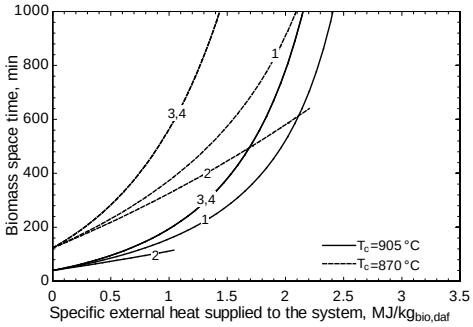

Fig. 2.7. Biomass space time of the different configurations (numbers over the lines) according to Fig. 2.2 when varying the SEH for different temperatures in the combustor.

Table 2.2 summarizes the pros and cons of each configuration in terms of circulation of active particles to the solar receiver, biomass space time and limitation in char conversion (i.e., limit in the amount of external heat that can be introduced into the process) due to requirement of char in the combustor for satisfying the energy balance of the process (see Paper II-Appendix A). It can be concluded that if the circulation of active particles to the solar loop is not of major concern, C1 is the most advantageous one, while C2 could be a good candidate if the combustor can be operated at low enough temperature for achieving significant char conversion in the gasifier.

Table 2.2. Summary of pros (tick) and cons (cross) of different configurations.

Configuration	1	2	3	4
Active particles in the receiver	✗	✓	✗	✓
Biomass space time	✓	✓	✗	✗
Limit in char conversion in the gasifier	✓	✗	✓	✗

2.3.3.2. Performance of the SDFBG coupled to a solar field

Fig. 2.8 shows the simulated performance of the DFBG operated with the solar energy collected by the reference solar field during the two DNI-peak days in summer and the two with the lowest DNI in winter [33].

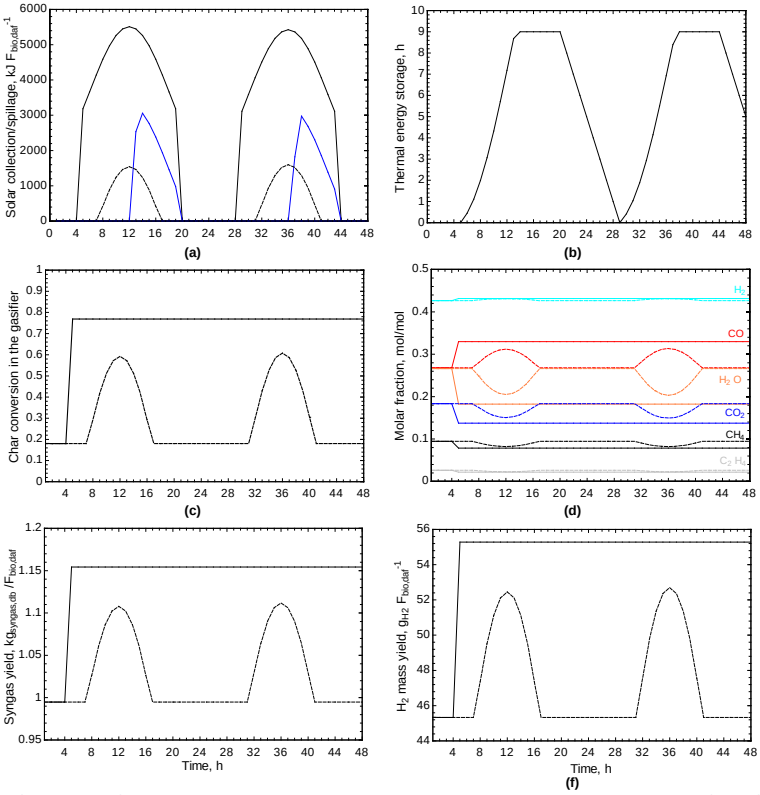

Fig. 2.8. Performance of the DFBG operating with a maximum char conversion in the gasifier of 78% when coupling with the solar side during two reference days in summer (—) and winter (---): (a) solar energy collected (black) and solar energy spilled (blue); (b) thermal energy storage (TES); (c) char conversion; (d) syngas composition; (e) syngas yield; (f) mass yield of H_2 in the syngas.

A nominal char conversion in the gasifier of 78% has been set for the simulations. Under this char conversion the system can operate during 9 h only supported by the reference TES (19.8 $MJ/F_{bio,daf}$). Fig. 2.8(a) compares the energy collected by the solar field in summer (with 15 light hours) and in winter (with 9 light hours), in the latter the low DNI does not allow reaching the required energy (2.2 $MJ/kg_{bio,daf}$), not even at the peak of the day. It is observed that during summertime there is sun spillage during 6 h, occurring when the TES in completely charged (Fig. 2.8(b)) and the solar field collects more energy than that required by the gasifier, while no solar spillage occurs during the winter. According to Fig. 2.8(b) it is possible to run the gasifier with a nine-hours TES in summer at the maximum conversion during 24 h, while there is not enough TES during winter and char conversion varies between 18% at nights (complete autothermal operation) and 60% during the peak of solar energy. Fig. 2.8(d–f) show the evolution with time of the syngas generated during winter and summer operation.

2.3.3.3. Solids circulation and gasification unit volume

A few DFBG has been operated so far [29], being the concept developed by Vienna University of Technology the first scaled into a commercial plant in Güssing [31]. This plant is referred to assess the proposed SDFBG. The DFBG in Güssing is comprised by a BFB gasifier and a circulating FB combustor. Solids circulation ratio between the reactors of 78 $kg_{sol}/kg_{bio,daf}$ has been reported [30,34]. The results obtained for the proposed SDFBG show solids circulation ratios below 60 $kg_{sol}/kg_{bio,daf}$ (even for the most unfavorable configuration of the external solids and completely allothermal operation). However, the mass inventory in a SDFBG operated at high allothermal conditions should be typically 10 times higher than in a DFBG. This value is obtained after comparing the estimated biomass space time of a SDBFG (800 min), according to Fig. 2.7, with that of the plant in Güssing (70 min, based on reported data [32]).

Overall, the proposed solar gasification technology presents huge potential for being scaled-up in the short to medium term taking the most of current state-of-the-art technologies of DFBG and solar particle receivers. However, the development of SDFBG requires from a carefully design of the gasification unit as well as from a flexible control of solids circulation to adapt the gasifier to changes in external heat supply.

Chapter 3. Fluid-dynamics of Dual Fluidized Bed Gasifier

In the previous chapter it was demonstrated that, compared to the state-of-the-art DFBGs, the design of the proposed SDFBG entails new features in the operation, being the main challenges: the control of solids circulation to allow the operation at different levels of solar external heat supply and, the higher inventory of solids required in the gasifier for operating at high solar heat supply (increasing the char conversion). The new operating conditions in SDFBGs require from a careful understanding of the fluid-dynamics of the system. A model of a conventional DFBG is developed to previously understand the hydrodynamic performance of current units, before extending the knowledge to solar conditions. The CFM at TU-Wien (Fig. 3.1(a)), one of the pioneering CFM developed for studying the fluid-dynamics performance of DFBGs [35,36], is taken as a reference and, experimental measurements from this unit are compared with the model results. The reference model is subsequently applied to a simpler geometry (Fig. 3.1(b)), for a more general analysis of the DFBG, including the comparison of performance when using a lower loop seal (LLS) instead of a pipe connection (Fig. 3.1(c)). The basics of the model accounting for a simple geometry are presented in the following section while, the detailed model developed to reproduced the measurements from the CFM can be found in **Paper III**.

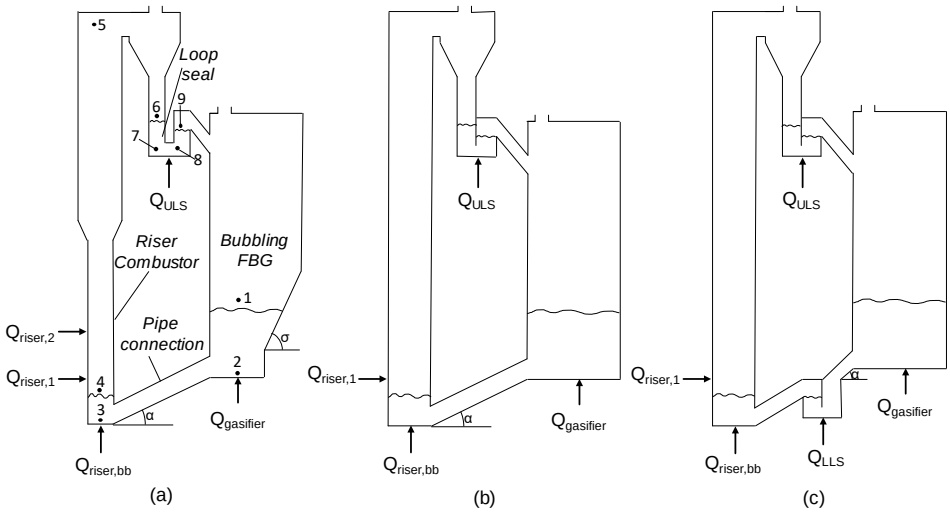

*Fig. 3.1. Sketch of the DFBs modelled (the actual dimensions are detailed in **Paper III**): (a) reference case from the CFM at TU-Wien; (b) simplified geometry based on (a); (c) simplified geometry replacing the connection pipe with a loop seal.*

3.1. Model description

The model of a DFBG consists of the fuel-conversion units (riser and gasifier), a cyclone for separating the particles, a loop seal, and lower pipe connecting the riser and the gasifier for the solids circulation. The model calculates the pressure and solids distribution along the system, as well as the solids flux for a given geometry, fluidization gas flowrates, total solids inventory and physical properties of the bed material.

The fluid dynamics model rests on two conditions that are approximately fulfilled in any circulating fluidized bed: (i) the efficiency of the cyclone at the riser outlet is assumed to be unity therefore, for a given operating conditions, the mass inventory is constant within the system, Eq. (3.1) and (ii) the difference of pressure between two points is equal to the pressure drops throughout the way between them, Eq. (3.2). Moreover, the pressure drop across the opening of the loop seals is neglected (this is contestable and is deeply discussed in Chapter 4), and that of the pipe connecting the ULS with the gasifier, together with the solids inventory in the cyclone are neglected.

$$W_T = W_{gasifier} + W_{pipe/LLS} + W_{riser} + W_{ULS} \tag{3.1}$$

$$\Delta P_{gasifier} + \Delta P_{pipe} = \Delta P_{riser} + \Delta P_{cyclone} \tag{3.2}$$

Eq. (3.2) turns into Eq. (3.3) when considering the LLS instead of the pipe connection,

$$\Delta P_{gasifier} + \Delta P_{SC,\,LLS} = \Delta P_{RC,\,LLS} + \Delta P_{riser} + \Delta P_{cyclone} \tag{3.3}$$

3.1.1. Gasifier

The inventory of solids and pressure drop across the gasifier are given by Eq. (3.4) and (3.5) where the only unknowns are the height (h) of the bed and the voidage (ε) of the bubbling bed.

$$W = \rho_p (1-\varepsilon) h A \tag{3.4}$$

$$\Delta P = \rho_p (1-\varepsilon) h g \tag{3.5}$$

ε is calculated considering the bubble fraction (δ) and the porosity of the emulsion at minimum fluidization (ε_{mf}):

$$\varepsilon = \delta + (1-\delta)\varepsilon_{mf} \tag{3.6}$$

The bubble fraction is estimated according to a model based on the modified two-phase theory considering the throughflow, after applying the correlation of Darton [37] and using experimental data of a stationary bubbling fluidized bed [38],

$$\delta = \frac{1}{1 + \dfrac{1.3(0.15 + u_0 - u_{mf})^{1/3}}{0.26 + 0.7e^{-3300\,d_p}}(u_0 - u_{mf})^{-0.8}} \tag{3.7}$$

The model accounts for the variation of the bubble fraction along the bed if the gas velocities change according to the geometry of the unit. The superficial velocity includes not only the air fed to the gasifier ($Q_{gasifier}$) but also the gas flowing through the lower pipe connection.

3.1.2. Connection pipe

An approach to solve the lower connection is assuming that it operates under moving bed regimen with a downwards flow of solids and, a gas than can flow either upward or downward depending on

the operating conditions (defined positive upward). Under this assumption, the momentum balance along the pipe, assuming a two fluid formulation at steady state can be applied. The momentum equation of the solid phase after neglecting the acceleration term and the spatial integration along the length of the pipe is

$$(1-\varepsilon)\frac{\Delta P}{L} = \rho_p(1-\varepsilon)\,g\sin(\alpha) - \beta(u_s + u_g) - \lambda\frac{u_s^2}{2}\rho_p(1-\varepsilon)\frac{A_{wall}}{A} \tag{3.8}$$

where the terms on the right refer to the weight of solids, the gas-solid drag force, and the solids-wall friction force. The latter is assumed following the approach presented in [35], where λ is the solids-wall friction coefficient as defined in Table 3.1, obtained after correlating experimental measurements assuming fluidized conditions. A fairer treatment would require a specific solids-wall friction coefficient for the moving bed flow. However, there is no way to correlate that coefficient in the literature since the friction relation for a granular material does not follow the same behavior as a simple fluid. In general, for moving bed flow a cross-pipe component of particle weight creates granular stresses between the particles and the pipe wall, requiring the use of at least one additional term. This is widely discussed in [39].

The momentum equation of the gas phase is given by Eq. (3.9) when neglecting the contribution of the acceleration, the weight of the fluid (gas) and the friction force with the wall, rearranging and substituting the differential term.

$$\varepsilon\frac{\Delta P}{L} = \beta(u_s + u_g) \tag{3.9}$$

In the equations above the parameter β accounts for the gas-particle interaction, which can be estimated with the Ergun equation (Eq. (3.10)) when the porosity in the system is below 0.8 [21].

$$\beta = 150\frac{(1-\varepsilon)^2}{\varepsilon}\frac{\mu_g}{\phi\, d_p{}^2} + 1.75(1-\varepsilon)\frac{\rho_g}{\phi\, d_p}\left(u_s + u_g\right) \tag{3.10}$$

The actual gas velocity and the solids velocity are given by,

$$u_g = \frac{u_0}{\varepsilon} \tag{3.11}$$

$$u_s = \frac{F_s}{\rho_p(1-\varepsilon)A} \tag{3.12}$$

Assuming a bed voidage equal to that at incipient fluidization, the rest of parameters in Eqs. (3.8)-(3.10) are known data so, the model can be solved giving the pressure drop along the pipe connection and the actual gas velocity through the pipe, u_g (note that the solid velocity, u_s, is related to the net solids circulating flow throughout the system, F_s, which is constant at steady state).

Most of author simplify this model [35,40] and calculate the gas velocity through the pipe by considering its operation under fluidized flow at incipient fluidization. Both modelling approaches are analyzed in **Paper III** leading to very similar results in terms of pressure drop (i.e., solids circulation) but different actual gas velocity through the pipe. This aspect is crucial in an actual DFBG where the gas leakage between unit needs to be avoided and the accurate modelling becomes a must to assess the limit in gas and solids flowrates to avoid the leakage. Moreover, the actual operation regime of the connection pipe is controversial being even probable the existence of a non-homogenous gas-solids pattern (where the gas flows upwards over the solids flowing downwards).

The mass of solids in the pipe is calculated in a similar way to Eq. (3.4) accounting for the geometry of the pipe and the assumed bed voidage.

3.1.3. Lower loop seal

Using a lower loop seal appears as an advantageous option when compared to the lower pipe connection. These aspects are widely discussed in Section 3.5 and Chapter 4.

The adopted model divides the loop seal in two regions, the supply chamber (SC, considering the downcomer as an extension of the SC) and the recycle chamber (RC) according to Fig. 3.2. The total flowrate of steam introduced (Q_{LLS}) is divided into that going through the RC (Q_{RC}) and that going through the SC (Q_{SC}). Both, the solids and gases in the RC flow upward while in the SC the solids flow downward while the gas can flow upward or downward depending on the operating conditions (defined positive upward, Fig. 3.2).

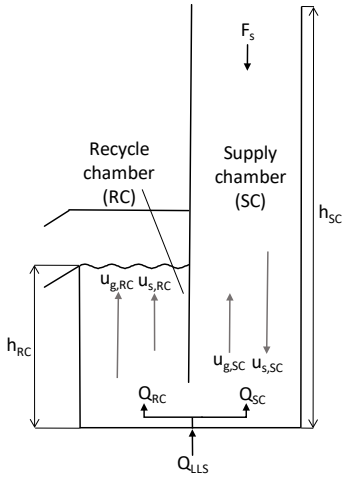

Fig. 3.2. Solids and gas velocities and fed gas distribution in the two chambers of the loop seal (downcomer is considered as an extension of the SC in this sketch).

The RC needs to be always fluidized to allow the solids circulation thus, the pressure drop, $\Delta P_{RC,LLS}$, is given by the hydrostatic pressure (as in Eq. (3.5)) of the head of solids along the RC up to the weir (h_{RC}, given by the geometry). The bed voidage in the RC (ε_{RC}) can be estimated considering the bubble fraction (δ) as in Eq. (3.6); a bubble fraction equal to zero represents the operation of the RC under incipient fluidization. The expansion of the bed can be calculated according to any expansion model for bubbling beds, as that from Eq. (3.7), but considering the superficial gas-solids relative velocity, $(u_{g,RC}-u_{s,RC})\varepsilon_{RC}$, for accounting the existence of a net flow of solids.

The SC can operate under fluidized or moving bed regime depending on the operating conditions. There is a critical velocity defined in Eq. (3.24) , comparing the relative superficial velocity with the minimum fluidization velocity: a positive critical velocity means that the SC is fluidized, while a negative value means that it is in moving bed regime [41].

$$u_{critic} = (u_{g,SC} + u_{s,SC})\,\varepsilon_{SC} - u_{mf} \tag{3.13}$$

According to this premise, if the bed is fluidized the pressure drop, $\Delta P_{SC,LLS}$, is estimated according to Eq. (3.5)) as the hydrostatic pressure of the head of solids along the height of the

downcomer (h_{SC}, given by the geometry); while if it is under moving bed flow the pressure drop is estimated from Ergun equation according to Eq. (3.9) but accounting for h_{SC}.

The bed voidage in the SC can be regarded, as a first approach, constant and equal to that at minimum fluidization conditions both, under moving and fluidized flow. Operating the SC above incipient fluidization is never desired for actual practical operation (since in CFB units leads to a decrease in the cyclone efficiency whereas in DFB systems it affects to the composition of the reacting gases) so the expansion of the SC when fluidized is not considered in the model.

The actual gas and solids velocities in both chambers are defined as in Eqs. (3.11) and (3.12), respectively, while the superficial velocities are given by considering the gas flowing through each chamber (equal to the total fed gas, Eq. (3.16)) and the cross section,

$$u_{0,RC} = \frac{Q_{RC}}{A_{RC}} \tag{3.14}$$

$$u_{0,SC} = \frac{Q_{SC}}{A_{SC}} \tag{3.15}$$

$$Q_{ULS} = Q_{SC} + Q_{RC} \tag{3.16}$$

An additional equation is needed to solve this model and stablish the gas split between the chambers and the downcomer height. The closure relation for this model is a matter of discussion, being the motivation of the experimental work in **Paper IV**. Since there is no general enough relation for closing the model, in **Paper III** the gas distribution was treated as a parameter, R_{RC}, which establishes the amount of gas flowing through the RC to that fed to the loop seal (Eq. (3.17)). The implications of this assumption are assessed in Section 3.5.

$$R_{RC} = Q_{RC} / Q_{ULS} \tag{3.17}$$

Therefore, once R_{RC} is set, the model can be solved and the pressure drop through both chambers determined. The inventory of solids in the loop seal is calculated as in Eq. (3.4) both for the RC and the SC.

3.1.4. Riser

The riser is modelled with a dense bottom bed, a transition or splash zone, and a transport zone. Part of the air is introduced through the bottom and the rest is added along the column (primary and secondary air) [35,42], as depicted in Fig. 3.1.

The dense bottom bed is modelled like the bubbling fluidized bed in the gasifier, i.e. using Eqs. (3.6) and (3.7) to estimate the porosity of the bed. The pressure drop and mass of solids in the dense zone are estimated as in Eqs. (3.4) and (3.5), where the height of the dense zone is not an input, but calculated by the model.

Above the dense bed there is a transition region (splash zone) with a high down-flow of solids falling back to the bed. The region downstream of the splash zone (transport zone) is characterized by solids concentrations much lower than in the splash zone and with a less pronounced decrease with height. Along the transport zone there is an upflow of solids in the core with a net lateral flow to the solids film downflowing along the walls [43]. These observations have motivated application of core-annulus models. However, there is no clear agreement on how to estimate the solids profile along these two zones, so semi-empirical models valid for specific operating conditions have been used [26,44–46]. In 1D models, the mean solids concentration along the freeboard (splash and transport zone) decays exponentially with height as described by the simplified model [47,48]:

$$\rho(h) = \rho_{TDH} + \left(\rho_{h=0} - \rho_{TDH}\right)\exp(-a\,h) \tag{3.18}$$

where $\rho_{h=0}$ is the solids concentration at the top of the dense zone, a is the decay coefficient, and ρ_{TDH} is the solids concentration at a height above the dense bed (h) which is higher than that at the total disengagement height (TDH) calculated according to Eq. (3.19).

$$\rho_{TDH} = \left(1-\varepsilon_{TDH}\right)\rho_p = \frac{E_\infty}{\left(u_0 - u_t\right)} \tag{3.19}$$

The decay coefficient, *a*, is the most uncertain parameter when modelling the solids distribution along the riser. A great deal of observations suggests that the decay constant increases with increasing particle size (particles are more likely to change direction and return to the dense bed), and decreases with the gas velocity (particularly for fine particle systems). These aspects have been interpreted in terms of a deposition coefficient giving the rate of particle transfer from the gas core to the falling particle film [49]. Recommendations for the value of the decay factor based on measurements are reported [50,51]. Kunni and Levenspiel [48] gathered data from literature to come up with Eq. (3.20), while Johnsson and Leckner [45] proposed Eq. (3.21) to fit the decay factor in the splash zone of a CFB boiler

$$a\,u_0 = C \tag{3.20}$$

$$a\frac{u_0}{u_t} = C \tag{3.21}$$

Although Eq. (3.21) is an empirical way to fit measurements, it is merely an extension of Eq. (3.20) taking into account the effects of particle diameter (and using the ratio u_0/u_t reported by [50] when studying the decay factor). Eq. (3.21) must be applied with caution when scaling up, since the vessel width is not accounted for, although it has been observed to influence the decay constant (rising agglomerates are more likely to hit the wall surface and be removed from the rising gas stream in narrower columns). A reasonable practice is to adjust the constant *C* with measurements for a given set of operating conditions (mainly gas velocity, particle size and column width). In this work we have modelled the decay factor using Eq. (3.21) but taking different values of the constant *C* for the splash zone and the transport zone (see Table 3.1). The value of *C* along the transport zone resulted from fitting to minimize the error of all the measurements shown in Fig. 3.3, while that of the splash zone was taken from [42]. In the model, the splash zone is defined as the region where the gas velocity is lower than the terminal velocity of a particle. The transport zone is assumed to extend itself from this point forward. Note that the superficial velocity in the riser considers both the air fed to the riser and the gas flowing through the lower pipe connection.

The solids density profile is estimated with Eq. (3.18) and, if the momentum losses due to wall friction and solids acceleration can be neglected as compared with the static head of solids, the pressure drop from the height of the dense bed to the top of the riser is estimated according to Eq. (3.22).

$$\Delta P = g\int_{h=0}^{H} \rho(h)\,dh \tag{3.22}$$

The effect of the solids acceleration within the momentum losses along the riser was assessed in **Paper III**. Results lead to discrepancies below 5% (for the worst scenario) when compared with the results of the model neglecting the acceleration.

The mass of solids along the splash zone and the transport zone is obtained from Eq. (3.23), while the total pressure drop and solids mass inventory in the riser result from adding the pressure drop and solids inventory of the dense zone to those of the splash and transport zones. The discretization of the solids distribution along the riser for accounting with lateral aerations and changes in the geometry along the column are assessed in **Paper III**.

$$W = \frac{\Delta P\, A}{g} \tag{3.23}$$

The solids flux circulating within the DFB, G_s (kg m^{-2} s^{-1}), is

$$G_s = F_s / A_{riser,top} \tag{3.24}$$

$$G_s = \rho_p (1-\varepsilon_{top})\, u_{s,top} \tag{3.25}$$

since the highly diluted region at the top of the riser allows assuming that the slip velocity equals the particle terminal velocity [48] and therefore, the solids velocity can be directly estimated as

$$u_{s,top} = \frac{u_0}{\varepsilon_{top}} - u_t \tag{3.26}$$

ε_{top} is the porosity at the outlet point of the riser (estimated from Eq. (3.18)).

3.1.5. Cyclone

The pressure drop across the cyclone is estimated using an empirical correlation, where the parameter ξ is mainly dependent on the cyclone geometry and was fitted in [35] for the reference unit and, the gas velocity refers to that at the top of the riser

$$\Delta P = \xi\, \rho_g\, u_0^2 \tag{3.27}$$

3.1.6. Upper loop seal

The estimation of the solids inventory (and pressure drops) in the ULS requires from a pressure balance since the height of solids in the downcomer (h_{SC}) is unknown. Actually, if both chambers are opened to the same environment and the ULS is operated just as a solids circulation device, i.e., both chambers are fluidized (assuming the same bed voidage) the height of the SC can be assumed as equal to that of the RC without leading to much error.

Considering the general model, and the gasifier and the riser-combustor opened to the same environment through the gas exit of the cyclone and the exit of the produced syngas, (i.e., P_6=P_9, referred to Fig. 3.1(a)) the pressure balance is given by,

$$\Delta P_{SC,ULS} = \Delta P_{RC,ULS} \tag{3.28}$$

Once R_{RC} is set, the model can be solved and the height of solids in the downcomer and the inventory in the loop seal determined.

Table 3.1. Summary of model parameters.

Parameter		Value/Correlation	[Ref]
λ	solids-wall friction coefficient	$3.5/u_{s,pipe}$	[15]
E_∞	elutriation constant	Colakyan & Levenpiel	[36]
ξ	constant dependent on the cyclone geometry	30	[15]
u_{mf}	minimum fluidization velocity	Grace	[37]
ε_{mf}	minimum fluidization porosity		
u_t	terminal velocity	Haider & Levenspiel	[38]
C	decay constant	splash zone: 10 transport zone: 4.2[1]	[16]
R_{RC}	gas flowing through the recycle chamber/total gas fed	0.5	-

[1]Obtained after minimizing the error of the measurements from the CFM at TU-Wien presented in Fig. 3.3, and used in section 3.2 (a rounded value of 4 was used when studying the performance of the system)

3.2. Comparison of model results with measurements

The model predictions are compared with measurements from the CFM at TU-Wien, a perspex CFM of the 8 MW_{th} biomass gasifier demonstration plant in Güssing, Austria. Experiments from [35,42] were carried out by varying the total solids inventory, total air flowrate fed to the riser, as well as the air staging along the riser within the ranges presented in Table 3.2 (the fluidization of the gasification unit was held constant as it was proved not to affect the solids circulation). Tests were conducted by measuring the pressure in each section of the CFM as well as the solids circulation rate by stopping the aeration of the loop seal and measuring the increase in the level of solids over the time. The experiments from [52] were conducted varying the bed pressure in the gasifier by adding bed material into the system for three total air flowrates fed to the riser, while keeping constant the air staging.

The geometry of the DFBG CFM (Fig. 3.1(a)) and that of the simplified sketch used for the analysis (Fig. 3.1(a-b)) are detailed in **Paper III**.

Table 3.2. Bed material, fluidizing agent and operating conditions of the tests and the reference case used for the analysis.

		Tests CFM	Reference case
Bed material		Bronze spheres	Bronze spheres
Size, d_p	μm	119	119
Sphericity, ϕ		1	1
Density	kg m^{-3}	8750	8750
Fluidizing agent		Air	Air
Temperature	ºC	20	20
Operating conditions			
Total inventory, W_T	kg	105-130	105
Total gas flowrate fed to the riser, $Q_{riser,t}$	Nm^3/h	250-400	300 (4.18 m/s)
Air supply to bottom bed, $Q_{riser,bb}$	Nm^3/h	20-60	60
Secondary to total air ratio, $Q_{riser,2}/Q_{riser,t}$		≈ 0.15-0.5	0.2[1]
Gas flowrate fed to the gasifier, $Q_{gasifier}$	Nm^3/h	47	47 (0.23 m/s)
Gas flowrate fed to the ULS, Q_{ULS}	Nm^3/h	4.5-6	1.15 u_{mf} [2]

[1] Only applying to Fig. 3.1(a)
[2] Referred to the relative gas-solids superficial velocity

Fig. 3.3 compares the results of solids flux given by the model with the measurements from the CFM at TU-Wien presented in [35]. It can be seen in Fig. 3.3(a) that most of the data points are scattered over a deviation of ±20% using a simpler and more general model of the transport zone compared to that in [35]. The results from the model developed here compare better with measurements than those from the previous model; a significant improvement is seen in the lowest range of solids flux (corresponding to the lowest air flowrate fed to the riser). Fig. 3.3(b) compares the same data but against the total air flowrate fed to the riser, showing not only the good capability of the model to predict the trend of the measurements for the whole range of operating conditions, but also the effect of the riser gas velocity and the total solids inventory over the solids flux. It is clearly observed that the aeration has a huge impact over the solids flux while the effect of the solids inventory seems to be lower.

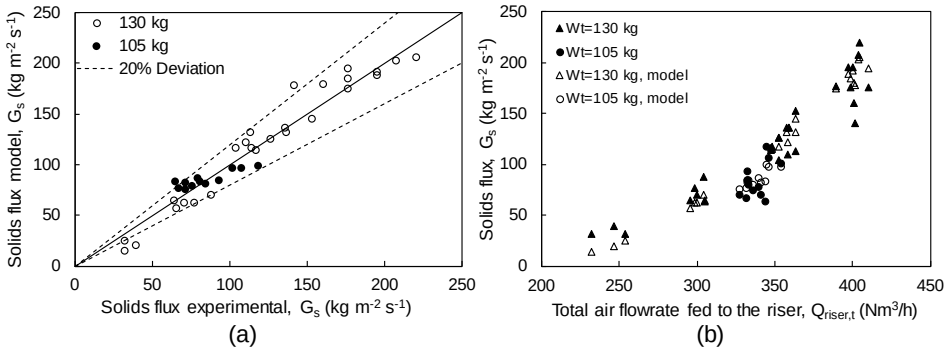

Fig. 3.3. Comparison of the solids fluxes given by the model with measurements from the CFM at TU-Wien with two different solids inventories and riser air flowrates ranging from 250 to 400 Nm^3/h, as represented in (b); tests made under different distributions of the air through the bottom, primary and secondary injections.

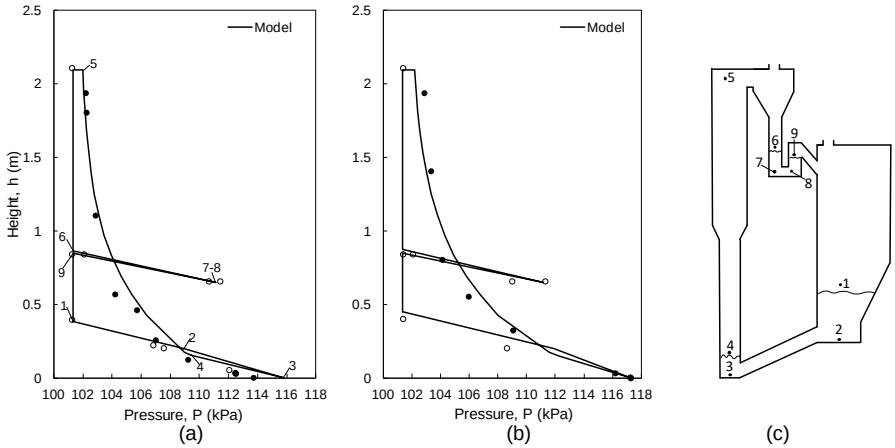

Fig. 3.4. Pressure loops obtained by the model compared with measurements from the CFM at TU-Wien: (a) W_t=105 kg, $Q_{riser,t}$=353.5 Nm^3/h, $Q_{riser,2}/Q_{riser,t}$=0.18, $Q_{riser,bb}/Q_{riser,t}$=0.06; (b)W_t=130 kg, $Q_{riser,t}$=396.8 Nm^3/h, $Q_{riser,2}/Q_{riser,t}$=0.5, $Q_{riser,bb}/Q_{riser,t}$=0.15 (solid circles represent measurements from the riser, while open circles those from the rest of the system; the point at height 0 m was not measured but estimated with the porosity given by the model for the dense zone of each test; in (a) numbers represent the pressures given by the model for points shown in (c).

The pressure profiles predicted by the model are compared with measurements in Fig. 3.4 for two different operating conditions. It can be seen that the model captures well enough the general trends of the measured profiles, giving a coherent behavior when increasing the solids inventory (i.e., higher maximum pressure is reached in Fig. 3.4(b) compared to Fig. 3.4(a)). The model also presents a good agreement with measurements from [40], in Fig. 3.5, where the total inventory of solids is predicted for a fixed pressure drop in the gasifier. Further discussion on the accuracy of the model when representing the data from the CFM, together with a sensitivity analysis of the parameters of the model are presented in **Paper III**.

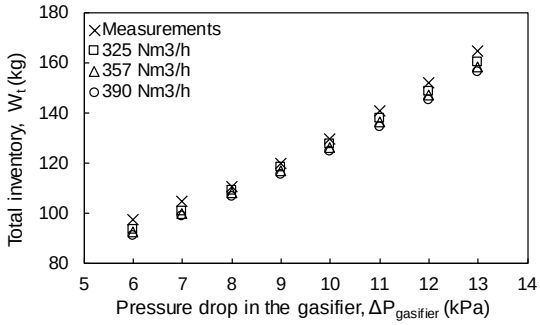

Fig. 3.5. Total solids inventory predicted by the model against pressure drop in the gasifier for three total-air flowrates fed to the riser ($Q_{riser,2}/Q_{riser,t}$=0.23, $Q_{riser,1}/Q_{riser,2}$=3) compared to measurements from [52] *(it is not possible to distinguish the small difference within the total inventory for the measurements under different aerations into the riser).*

The robustness of the model was assessed by a sensitivity analysis of the parameters. Results shown that the only parameters having a significant sensitivity in the model predictions are the particle terminal velocity and the decay constant of the transport zone in the riser. Special attention must be paid when selecting the particle decay constant since the available data is scarce and vary widely between risers.

3.3. Analysis of the DFBG fluid-dynamics performance

The simplified geometry sketched in Fig. 3.1(b) was used to assess the performance of the DFBG. Fig. 3.6(a) shows that the solids flux is more sensitive to changes in the riser aeration than in the solids inventory: 60% rise in the solids flux can be reached by increasing the air velocity by 15% (over the reference case, $u_{0,riser}$), while an increase in the solids inventory of 60% only produces an increase in the solids flux of 17%. This behavior (experimentally verified in Fig. 3.3(b)) is explained in Fig. 3.6(b) where it is seen that an increase of 15% over the total solids inventory (of the reference case, i.e. from 105 kg to 120 kg) leads to an increase in the gasifier solids inventory of 11.4 kg but only an increase of 3.6 kg in the riser. The reason of this distribution is the difference in the cross sectional areas of the gasifier and riser, requiring a higher amount of solids in the gasifier (larger diameter) to balance the increase in pressure drop in the riser. On the other hand, Fig. 3.6(b) shows that the higher the gas velocity in the riser, the higher the solids displacement from the riser to the gasifier.

Fig. 3.6(c) shows the influence of the geometry on the solids circulations and solids residence times in the system. It is shown that for keeping constant the solids flux at 100 and 130 kg m^{-2} s^{-1} while increasing the total solids inventory of the system from 100 to 160 kg, the diameter of the gasifier needs to be increased by 60 and 68%, respectively. On the other hand, the increase in the total inventory, keeping constant the solids circulation, leads to a higher accumulation of solids in the gasifier resulting in longer space time of the reactive particles (fuel and char) in the gasifier of

a real unit. It is observed that the space time (ratio of the mass inventory of the gasification unit to mass flowrate of fuel fed to the gasifier), is increased 2.5 and 2.8 times for the solids fluxes considered. Note that for a given total solids inventory, an increase in the solids flux requires a larger amount of solids in the riser, leading to a reduction of the amount of solids in the gasifier and, consequently, to balance the pressure loop, a reduction of the diameters ratio (i.e., a smaller diameter of the gasifier is required for compensating the higher pressure drop along the riser). Finally, Fig. 3.6(d) demonstrates that the particle size has a huge impact on the solids circulation, being the effect more significant as the gas velocity in the riser is increased. Therefore, the selection of the particle size of the bed material is extremely important for the control of the solids circulation in a DFBG.

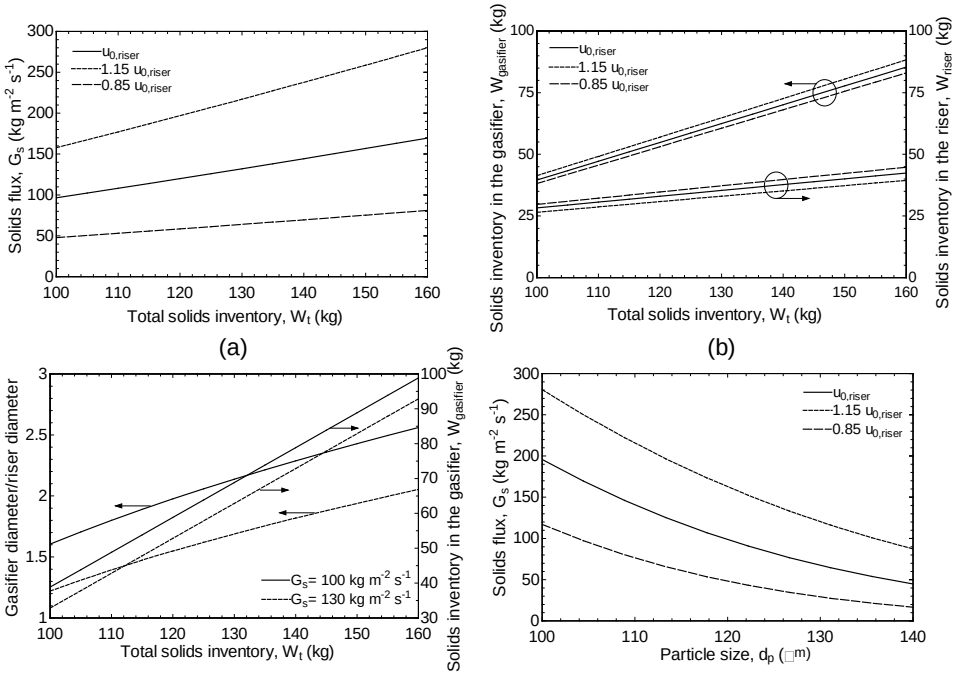

Fig. 3.6. Analysis of the performance of a DFBG (Fig. 3.1(b)): (a) effect of the total solids inventory and total aeration in the riser over the solids flux; b) distribution of solids between the gasifier and riser for the operation under different solids inventories and riser gas velocities; (c) relation of diameters gasifier/riser (the diameter of the riser is kept constant) and solids inventory in the gasifier for keeping constant the solids flux at 100 and 130 kg m^{-2} s^{-1} while varying the total solids inventory; (d) effect of the particle size over the solids flux. The operating conditions not specified in the figures are those of the reference case (Table 3.2).

3.4. Solids circulation in a SDFBG under high allothermal operation

As concluded in Section 2.3.3.3, the solids inventory in the gasification unit of a SDFBG, operating under a high share of solar external heat, is typically 10 times higher than in a conventional DFBG. The effect of increasing the solids inventory in the gasifier on the solids flux is shown in Fig. 3.7. The solids inventory given by the model under the operating conditions of the reference case (Table 3.2) for the system in Fig. 3.1(b), is used as a reference for the solids inventory in the gasifier of a conventional DFBG. As expected, the increase in the solids inventory in the gasifier leads to an increase in the solids circulation due to the higher inventory required in the riser to maintain the pressure balance of the system. It is observed that, operating the system with the diameter of the

gasifier of the reference case ($d_{gasifier}$), under the typical inventory of solids required by an SDFBG operated at high allothermal conditions, would lead to an unreasonable solids flux. Therefore, as shown in Fig. 3.7, the gasification unit of the new SDFBG needs to be larger in diameter to meet both requirements: providing enough volume for char conversion and operating under a solids flux that is in the order of those of the conventional DFBG. As shown in Fig. 3.7, a system with a gasifier three times larger in diameter allows keeping the solids flux around the values of the operation of the conventional DFBG ($W_{gasifier,SDFBG}/W_{gasifier,DFBG}$=1, G_s=100 kg m^{-2} s^{-1}) for the solids inventories required at high allothermal conditions in the gasifier of an SDFBG.

Note that, in this new design, although keeping the solids circulation under reasonable values, it increases with the solids inventory in the gasifier (i.e., with the SEH). However, the opposite behavior (the internal solids circulation tends to zero while increasing the SEH) was obtained from the analysis of the SDFBG presented in **Paper II** (see Fig. 2.6(a))), for C1 and C2 (those identified as the best options for integrating the external solids circulation into the system). Therefore, in the new SDFBG, the adjustment of the solids flux to meet the heat demand of the gasifier coupled with the solar resource, needs from especial considerations, which are assessed in Chapter 5.

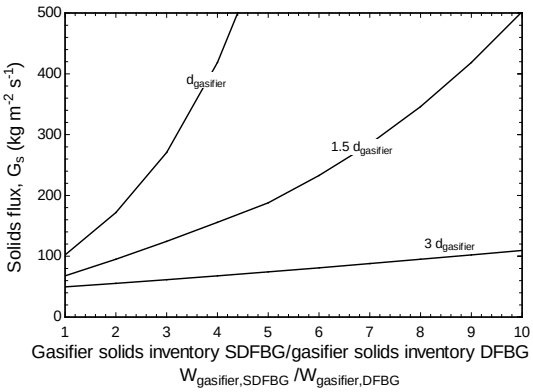

Fig. 3.7. Solids flux as a function of the ratio of inventories between the gasification unit of the partially allothermal SDFBG and the gasification unit of the autothermal DFBG for three gasifier diameters ($d_{gasifier}$=0.275 m) while keeping the gas velocity constant in the gasifier. Other operating conditions were kept as those of the reference case (Table 3.2).

3.5. Lower pipe connection versus lower loop seal

The performance of the DFBG in terms of the solids circulation is shown in Fig. 3.1 for a system with a lower pipe connection (a) and with a LLS (b). It is observed in both figures that, when increasing the fraction of air flowing through the RC in the ULS (i.e. decreasing the gas flow through the SC), the solids flux remains constant while the SC remains fluidized, but it decreases when the SC enters the moving bed flow (at high R_{RC}, since low gas circulates through the SC). The latter behavior is observed to a greater extension in the LLS, leading to a sharply decrease in the solids circulation as the SC gets into moving bed regime. Moreover, in the LLS there is a maximum in the solids circulation leading by the operation that keeps the SC under fluidized flow while maximizing the air flowing through the RC (since for a constant gas fed to the riser, the higher the gas flowing through the RC the higher the gas velocity in the riser). Note that the contribution of the gas flowing through the RC to the entrainment of solids in the riser is determined by the geometry. For instance, it is expected to be negligible in large CFB where the cross section of the loop seal is rather small compared to that of the riser. On the other hand, the gas fed to the riser could be theoretically compensated (by decreasing it) to keep the aeration constant while increasing the gas flowrate through the RC. Under this assumption, for a given operating conditions, it is expected the solids

circulation to be higher in the system with the lower pipe connection (provided that the solids-wall friction in the pipe lead to lower resistance than that of the LLS).

It is observed in Fig. 3.1(b) that for a given fraction of air through the RC of the ULS, when increasing the fraction of air through the RC in the LLS ($R_{RC,LLS}$) from 0.5 to 0.7 the solids flux considerably increases but, when $R_{RC,LLS}$ is further increased to 0.96, the obtained solids flux decreases below that at 0.5. The reason is that changing from 0.5 to 0.7 increases the air flowing through the riser (as more gas flows through the RC in the LLS) while the SC remains under fluidized flow while, at $R_{RC,LLS}$=0.96, although the gas going into the riser increases, the SC operates under moving bed flow limiting the solids flux. The same trend, but not with such effect on the solids circulation, is observed for a constant fraction of air through the RC in the LLS when increasing the fraction of air through the RC in the ULS ($R_{RC,ULS}$): from 0.5 to 0.7 both chambers in the ULS are under fluidized flow and the slightly increase observed in the solids flux results from the lower solids inventory in the ULS (due to the higher expansion of the RC) leading to higher inventory of solids in the riser; at $R_{RC,ULS}$=0.96 the SC of the ULS operates under moving bed flow and, a higher height of solids is required in the downcomer to give the required pressure drop leading to a lower inventory of solids in the riser and, therefore, to a lower solids flux.

The results clearly show that operating a DFBG with a LLS allows a wider control of the solids circulation (the loop seal acts as a non-mechanical valve) compared to that with a lower pipe connection. In a DFBG operated with two loop seals, the LLS is that allowing a wider control of solids circulation (although the ULS also provide some controllability). From the previous analysis it is concluded that, the better performance of the LLS as non-mechanical valve comes from the mechanism for controlling the solids circulation: in the LLS is made by direct changes in the pressure balance of the system while, in the ULS is related to the displacement of solids inventory from the riser. Therefore, the higher the ULS compared to the riser, the higher its availability to control the circulation of solids.

The use of an LLS instead of a pipe connection will be advantageous in the development of SDFBGs since, as previously concluded, they require from high flexibility and control of the solids flux, for meeting the heat demand of the gasifier when coupled with the solar field. Moreover, the LLS appears a safer option for reducing the gas leakage between unit compared to the lower pipe connection.

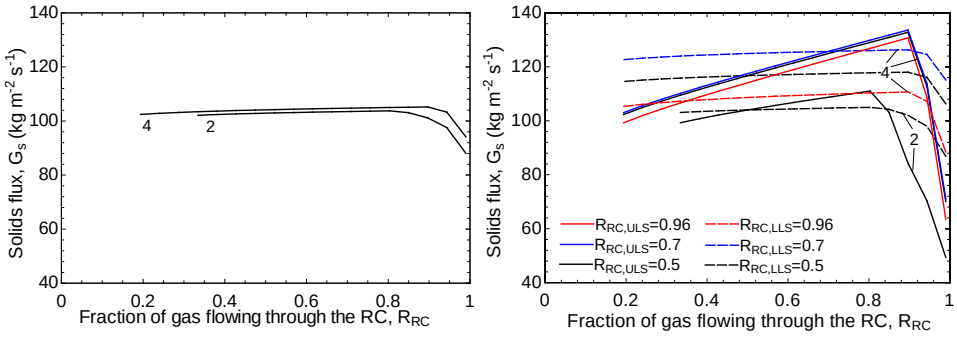

Fig. 3.8. Solids flux when varying the fraction of gas flowing through the RC under gas flowrates fed to the loop seals corresponding to 2 and 4 times the minimum fluidization velocity (not accounting for the circulation of solids). Results from (a) correspond with the system in Fig. 3.1(b) while those in (b) correspond with Fig. 3.1(c) where R_{RC} is varied in one of the loop seal keeping the other constant at 0.5.

Chapter 4. Fluid-dynamics of loop seal

It was demonstrated in Chapter 3 that loop seal devices play a key role in DFB systems both for avoiding the gas leakage and for controlling the solids circulation. Moreover, it was introduced the problem arising when trying to model and predict the performance of a loop seal unit. These issues were the motivation of this experimental study which was intended to shed light on a closure relation allowing to model the gas distribution along the loop seal and therefore, to optimize the design and operation of these devices within DFB units, as the SDFBG proposed in this thesis.

4.1. Theory

The operation of the loop seal as a non-mechanical valve takes places when the standpipe is under moving bed regime (also referred as transitional packed bed) and the pressure drop per unit length (pressure gradient) is controlled by the drag force between gas and solid particles, which depends on the gas-solids relative velocity. Under this operation, a change in the gas-solids relative velocity results in a change in the pressure gradient along the standpipe, which needs to reallocate the solids to keep the pressure balance around the CFB loop, leading to a change in the solids circulation. The range of solids circulation control of a non-mechanical valve is determined by the ability of changing the gas-solids relative velocity before it reaches the minimum fluidization velocity (related to the flow of solids). Therefore, the design of a loop seal as non-mechanical valve should promote the flow of gas through the SC, allowing to build a higher pressure drop in the standpipe and then a higher solids circulation.

It can be said that the gas distribution along the loop seal is the key parameter determining the performance of the system i.e., the flow state of the supply SC/standpipe/downcomer (usually regarded to be a dense bed in minimum fluidization or a moving bed) and the regulation capability of the solids circulation. This issue has been a matter of concern over the years when trying to model and predict the performance of loop seals.

The aeration mode has a great effect on the gas distribution along the loop seal and, although it has been treated in many works [53–55], clear conclusions on the operation of the loop seal under its simplest aeration modes are still faded. The experiments carried out in this work were intended to fill this gap.

When it comes to assess the performance of a loop seal by modelling, it was shown in Section 3.1.5 that a closure relation allowing to predict the gas distribution through the two chambers of the loop seal is lacked. None of the model developed up to now are general enough to predict the performance of loop seals. Those based on correlations [56,57] are only applicable to the units from which the correlated measurements were obtained, while those based on theoretical approaches [58,59] have failed in their attempts since they have not been able to catch the limiting factors

leading to the gas split between the chambers (key aspects as the aeration mode have been overlooked). The experimental work presented here clearly demonstrates that theoretical prediction of the operation of a loop seal requires from a more careful modelling effort than that paid by the models developed up to now.

A wide discussion on the different assumptions, studies and modelling approaches adopted by different authors is presented in **Paper IV**.

4.2. Experimental work

4.2.1. Experimental setup

The experimental setup was isolated from an existing CFB cold flow model to dedicatedly study the gas and solid motions in the different parts of the loop seal. The rig, presented in Fig. 4.1, consists of a hopper joined to a solids discharge system (pipe and valve for controlling the solids flux) and a loop seal joined to a cyclone which collects the circulating solids leaving the system into a bin. Two rotameters are used to control the gas flowrate separately, one to feed the gas to the supply chamber (SC) and another one to the recycle chamber (RC) (the wind boxes of the SC and RC are completely separated from each other). The gas leaving the cyclone, i.e., that passing through the RC, is measured by another rotameter, which requires from a valve at the inlet to stabilize the float. A measuring tape is set along the downcomer to measure the height of solids during the tests. Fifteen pressure taps are allocated along the loop seal. A data logger and a computer are used to continuously (every second) register the pressure measurements.

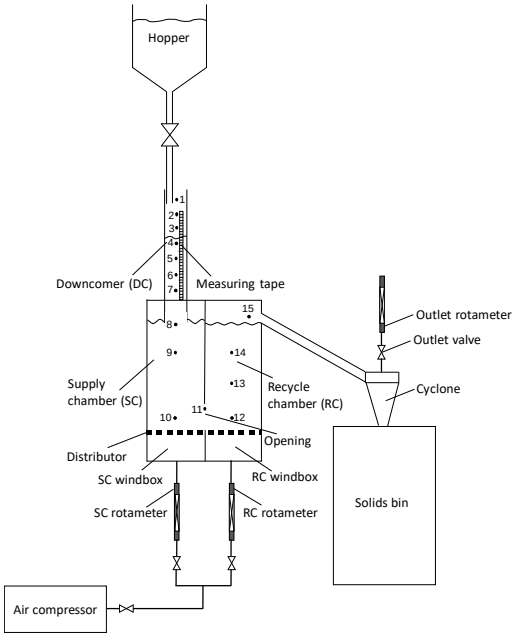

Fig. 4.1. Experimental rig (numbered dots represent the pressure taps; dot number 1 is never covered by solids so it represents the atmospheric ambient at which the SC is opened).

The downcomer is 0.093 m internal diameter, SC and RC have a cross section of 0.119x0.130 m^2 while the section of the opening is 0.130x0.055 m^2. The height of the SC above the distributor is 0.270 m and that of the RC until the discharging pipe is 0.155 m. The measuring tape is located just

above the SC but the downcomer is 0.060 m below this point (0.02 m along the junctions and 0.04 m inside the SC).

The bed material was glass beads with a particle size of 150-250 μm, a density of 2503 kg/m^3 (Geldart B) and an experimental minimum fluidization velocity at room temperature of 0.04 m/s. Air at room temperature was used as fluidizing agent.

4.2.2. Experiments

During the tests the solids flux was kept constant while varying the gas flowrate fed to the system as well as the aeration mode. Solids fluxes of 5, 10 and 15 kg m^{-2} s^{-1} (referred to the SC cross section) were tested at three different aeration modes (only RC, only SC and both chambers). The same gas flowrate was introduced through each chamber in experiments aerated under both chambers. For each test the pressure at taps presented in Fig. 4.1 was continuously measured and registered for two minutes of operation after reaching the steady state. The latter was considered to be attained when the height of solids in the downcomer reached a constant value in the measuring tape. The gas split into SC and RC was calculated by the difference between the introduced air and that leaving the system through the RC.

Two sets of tests were carried out: one with the outlet rotameter (and the outlet valve) for measuring the gas leaving the RC and, another, removing both, the outlet rotameter and valve, to assess the effect of this outlet constriction in the gas and solids distribution along the loop seal. In those tests carried out with the outlet rotameter, the outlet valve was kept always at the same position. A minimum of 2 tests were made for each operating conditions to guarantee the repeatability. The tests carried out (145 in total, 108 with the outlet valve and 37 without outlet valve) are summarized in **Paper IV**-Table 1.

4.3. Results and discussion

Experiments were carried out for constant solids fluxes varying the aeration flowrate. For a given solids flux, after a change in the air flowrate fed, the solids inventory in the system varied adapting the pressure throughout the unit to allow the operation under the new conditions. This operation gives understanding on the behavior of an isolated loop seal, but the gained knowledge is to be used to describe the performance of the loop seal connected to a CFB unit where (most of the times) the solids inventory is kept constant while the solids flux is the variable to be controlled. Experimental results obtained in the isolated loop seal under constant solids fluxes are presented in Section 4.3.1, while discussion on how this information is used in a loop seal coupled to a CFB unit is discussed in Section 4.3.2.

4.3.1. Experimental results

The gas split between the chambers of the loop seal can be understood by examination of Fig. 4.2. The gas flowrate through the RC (Fig. 4.2(a)) and SC (Fig. 4.2(b)) is plot as a function of the total gas flowrate fed into the loop seal for three solids fluxes and three aeration modes (SC, RC and both chambers). In agreement with previous studies [60], the solids flux has a direct effect on the gas distribution. For a given air flowrate fed to the loop seal, the air flowing through the RC increases as the solids flux is augmented, due to the higher amount of air dragged in the SC by the downwards flow of solids.

Furthermore, it is seen that the gas split in the loop seal strongly depends on the aeration mode. For a given total air flowrate fed to the loop seal, the highest gas circulation through the RC is obtained when aerating through the RC, and the lowest by aerating through the SC. For a given solids flux, increasing the air flowrate through the SC leads to an almost constant gas flowrate through the RC. It is only observed a considerable decrease when the SC gets fluidized, suggesting that once bubbles are formed in the SC, the gas finds lower resistance flowing through the bubbles

than going through the dense bed in the RC, resulting in a reduction of the gas circulation through the RC, even after increasing the total aeration. As expected, the aeration flowrate at which the SC gets fluidized is higher as the solids circulation is increased. When the loop seal is aerated through both chambers or RC the air flowing through the RC always increases with the increase in the total air flowrate.

Fig. 4.2(c) presents the flow of air circulating through the opening, which is defined as positive in the direction of the circulating solids i.e., from the SC to the RC. It is observed that, for a given solids flux, when the loop seal is aerated through the SC and through both chambers, the gas flowrate through the opening is almost constant and positive for all the gas flowrates tested. On the contrary, when the loop seal is aerated through the RC the gas circulates from the RC to the SC (excepting for the lowest aeration at a solids flux of 15, at which the gas is dragged from the SC to the RC) and it is higher as the air flowrate fed to the loop seal is increased.

It was observed that in tests aerating only through the SC, the RC was always a dense bed with no bubbles, while vigorous bubbling appeared as the gas flowrate was increased for the other aeration modes (RC and both chambers). This observation is evident from Fig. 4.2(d), where it is shown that, when aerating through the SC, the fluidization number in the RC (ratio of actual to minimum fluidization velocity) is well below 1.5 and it is practically constant as the aeration increases, whereas it greatly increases when aerating through the RC. However, bubbles are expected to appear in the RC when aerating only through the SC at high enough solids fluxes as a result of the gas dragging (this was not visualized in our experiments due to the limited range of solids fluxes tested).

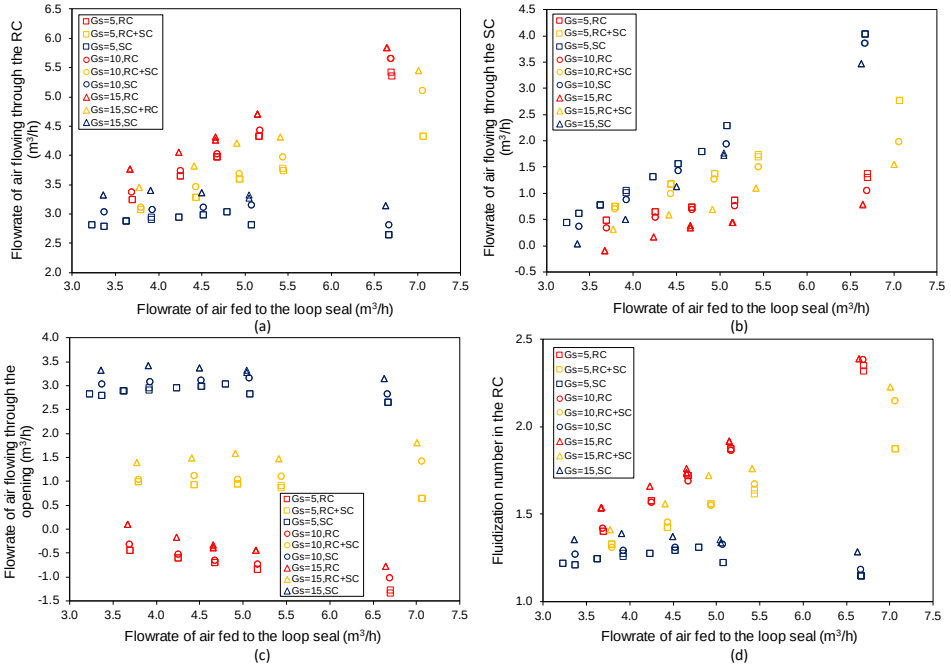

Fig. 4.2. Air flowing (a) through the RC, (b) through the SC and (c) through the opening, and (d) fluidization number in the RC (superficial gas velocity in the RC to minimum fluidization velocity considering the solids flux) against the total flowrate of air fed to the loop seal for tests with the outlet rotameter under different solids fluxes (shape of the marker) and aeration modes (color of the marker; RC: only RC, RC+SC: both chambers, SC: only SC).

A better understanding of the influence of aeration modes is obtained by analyzing Fig. 4.3 where the height of solids in the downcomer is presented for the three aeration modes tested. Note that the constriction introduced by the pressure drop of the valve prior to the outlet rotameter needs to be considered; logically, the pressure drop through the valve is higher as the gas flowrate circulating through the RC increases.

Fig. 4.3 shows that, for a fixed aeration flowrate, the height of the downcomer rises with the increase in the solids flux for any of the three aeration modes. In contrast, when increasing the aeration for a fixed solids flux, the height of the downcomer follows different behavior depending on the aeration mode: the height continuously decreases when the gas is fed through the SC and through both chamber (although not so significantly), while it presents a minimum when aerating through the RC. This behavior is not evident at all, but it is explained in detail as follows, related with the gas split according to the different aeration modes.

When the loop seal is aerated through the SC, for a given solids flux the amount of air flowing through the RC is almost constant (as shown in Fig. 4.2(a)) leading to a fairly constant pressure drop in the outlet valve and through the RC. Consistently, the gas circulating through the SC increases as it does the total air flowrate and so, the height of solids in the downcomer needs to decrease (Fig. 4.3) to maintain the pressure of the system under a constant value (according to the pressure drop at the RC side). It is also observed that the height of solids in the downcomer tends to a constant value at high gas flowrate since, once the SC gets fluidized, the pressure drop remains roughly constant with the air flowrate.

The aeration of the loop seal through the RC leads to the highest height of solids in the downcomer for a given flowrate of fed gas, as it is seen by comparison of Fig. 4.3(a) and Fig. 4.3(b). This is due to the low circulation of gas through the SC when aerating by the RC (Fig. 4.2(b)), which results in a higher height of solids to compensate the pressure drop of the system. The height of solids in the downcomer decreases with the increase in aeration flowrate through the RC, while the increase in the gas circulating through the SC leads to a higher pressure drop than that required to compensate the pressure drop introduced by the outlet valve. For higher aerations the pressure drop given by the outlet valve becomes so high that the increase in the gas circulation through the SC is not enough to compensate it and the column of solids starts building upwards, explaining the minimum found in Fig. 4.3(b).

As expected, an intermediate behavior is observed as the aeration is applied through both chambers. The height of solids in the downcomer Fig. 4.3(b) is in between of that obtained for the SC and the RC aerations. The trend of the solids height profile is closer to that obtained when aerating through the SC since, for all the air flowrates tested, the circulation of gas through the SC led to a higher pressure drop than that required to compensate the increase in pressure drop given by the outlet valve (leading to a decrease in the height of solids).

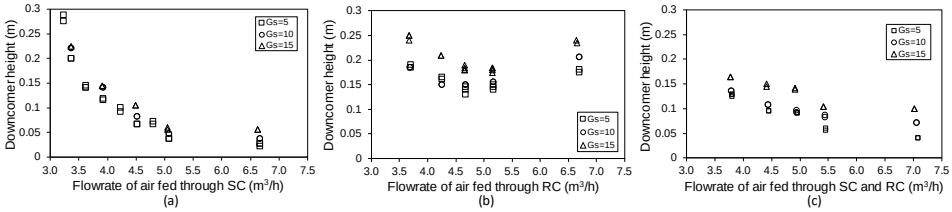

Fig. 4.3. Height of the downcomer (a, b, c) against the air fed through the different aeration modes for tests carried out with the outlet rotameter under the different solids flow rates.

According to the measurements from the gas circulation through the opening (Fig. 4.2(c)) the behavior of pressure drop through it (P_{10}-P_{12}) could be a priori anticipated: (i) a rather constant pressure drop should be measured when aerating through the SC/both chambers (since the gas

circulation is roughly independent of aeration fed for a given solids flux), and (ii) a negative and decreasing pressure drop should be measured while increasing the aeration through the RC (since more gas circulates from 12 to 10). However, as shown in Fig. 4.4(a), the actual behavior apparently differs from that expected. Despite the scattering of measurement, it is clearly seen that the pressure drop is higher when aerating through the SC and it decreases, for the three aerations modes, with the increase in the air fed to the loop seal. The latter contradicts statement (i). However, it is explained by considering the irregular gas-solid flow through the opening. At low aerations, the solids at the bottom of the SC are very compacted, favoring gas shortcuts instead of a homogenous distribution. As the aeration is increased, the solids in this zone are softened (somehow better lubricated), allowing for a better distribution of the gas through the cross section of the horizontal passage and the opening. When taking a shortcut, a given gas flowrate through the opening leads to a higher gas-solids relative velocity (equivalent to consider a narrower effective cross section) and so, to a higher pressure drop. The same gas flowrate under a homogeneous gas-solid flow distribution leads to lower gas-solids relative velocity resulting in lower pressure drop. Finally, it is observed that the trend of the pressure drop with the aeration through the RC is consistent with that expected in statement (ii), although the expected negative pressure drops were only registered for the highest air flowrate tested.

The ability of the different aeration modes to change the solids flux in a CFB unit is assessed in this work by the increase in the standpipe pressure gradient (see Section 4.3.2.1 for details on the operation of loop seals in CFB systems). This increase in the pressure gradient is evaluated by the change in the pressure drop measured between taps 10-8, which are always covered by solids. Measurements reported in Fig. 4.4(b) show that the pressure gradient through the SC increases for all the aeration modes but the highest slope is observed when aerating only through the SC. This implies that, in a CFB unit, the aeration of the loop seal through the SC allows controlling the solids circulation with the lowest aeration and solids inventory. The maximum solids flux given by the loop seal operated as a non-mechanical valve is that of the SC under fluidized regime (from this point forward there is no change in the pressure drop of the SC/downcomer), which is reached at around 5 m^3/s when aerating through the SC and 7 m^3/s when aerating through both chambers while, for the flowrates of air tested, it is never reached when feeding the air through the RC.

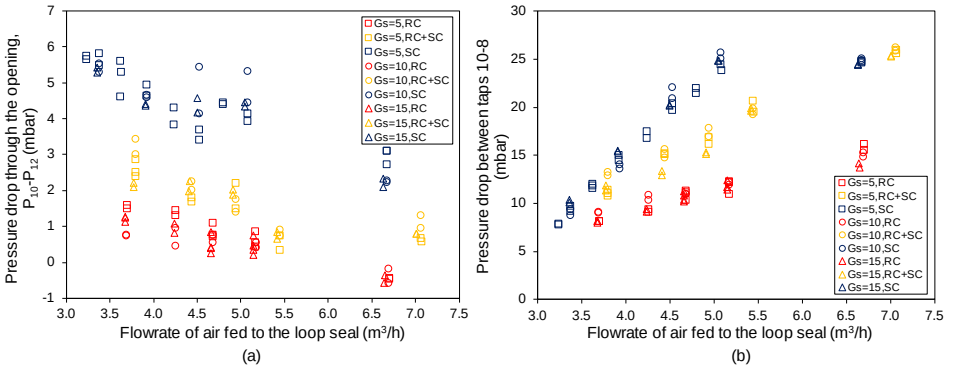

Fig. 4.4. (a) Pressure drop through the opening against the flowrate of air flowing through the opening and (b) pressure drop through the SC between taps 10-8 against the flowrate of air fed to the loop seal for tests with the outlet rotameter under different solids fluxes (shape of the marker) and aeration modes (color of the marker; RC: only RC, RC+SC: both chambers, SC: only SC).

Tests without outlet rotameter were conducted to compare the performance of the loop seal with and without restriction to flow at the exit of the recycle chamber (i.e., the difference of pressure drop (P_{15}-P_1)). Experimental measurements are reported in **Paper IV**-Section 4.1.2., a summary of the main conclusions is presented here.

In the absence of the restriction imposed by the outlet valve, the maximum pressure of the isolated loop seal rig either remains constant or slightly decreases (due to the RC bed expansion) as the gas flowrate fed to the loop seal is increased, but it never increases as it does when operating with the outlet valve. This implies that without outlet valve the height of solids in the downcomer always decreases with the increase in the aeration flowrate, even for the aeration through the RC. Moreover, the height of solids in the downcomer is lower in tests carried out without outlet valve as compared to those with valve, due to the lower pressure drop to be compensated.

Although accurate estimations on the gas distribution along the loop seal are not possible in tests without outlet rotameter, it appears clear from the comparison of the pressure drop measurements, that the performance of the loop seal follows the same trends with and without outlet valve. The conclusion is that, although the actual gas-solids distribution is affected by the pressure drop along the other components of the CFB loop, the pattern of the resistance of the loop seal unit to gas-solids flow (resistance curve) is characterized, to a large extent, by its geometry.

4.3.1.1. Gas-solids flow patterns in the operation and modelling of loop seals

The experimental results showed that the aeration mode, together with the geometry of the unit, establishes the distribution of the gas fed through the loop seal and, therefore, the performance of the loop seal under different aeration and solids circulation flowrates. It was shown that the non-homogeneous gas distribution and the appearance of stagnant zones of solids are essential to understand (and predict) the gas split between the chambers.

Fig. 4.5 and Fig. 4.6 show the non-ideal gas and solids flow patterns observed when operating the loop seal rig under mono-chamber aerations, SC and RC, respectively. The stagnant zone formed at the bottom of the SC is reduced with the increase in aeration through the SC until disappearing once it gets fluidized Fig. 4.5(a-c). At low solids flows the RC is a dense bed close to incipient fluidization, while bubbles start flowing close to the central baffle as the solids flow is increased, due to the higher contribution of the gas dragged by solids (Fig. 4.5(d)). Although not represented in figures, it is clear from Fig. 4.5(d) that when aerating through the SC the gas is spread into the RC through the upper part of the opening, leading to a lower stagnant zone in the RC. Fig. 4.6 shows that the operation of the loop seal when aerated through the RC is characterized by a significant stagnant zone in the SC, but a good gas distribution across the RC, leading to a vigorous bubbling as the aeration is increased. Although the death zone in the SC decreases both with increasing the aeration and the solids circulation, it always remains considerable (Fig. 4.6(c)). An intermediate behavior is obtained when aerating the loop seal through both chambers. The evolution of the stagnant zone in the SC of a loop seal equally aerated under both chambers was assessed in [41] by tracer solids, confirming our observations and measurements.

It is concluded that, independent on the aeration mode, there is always a stagnant zone in the SC while operated under moving bed flow. The size of the stagnant zone is reduced as the air flowrate and solids flow are increased but it only disappears when the SC gets fluidized (which only happens at high aeration rates fed through the SC). At this point the loop seal loses the ability of controlling the solids circulation; in other words, the operation of a loop seal as a non-mechanical valve always entails the presence of a death zone in the SC. On the contrary, stagnancies in the RC can be easily avoided providing some aeration through the RC.

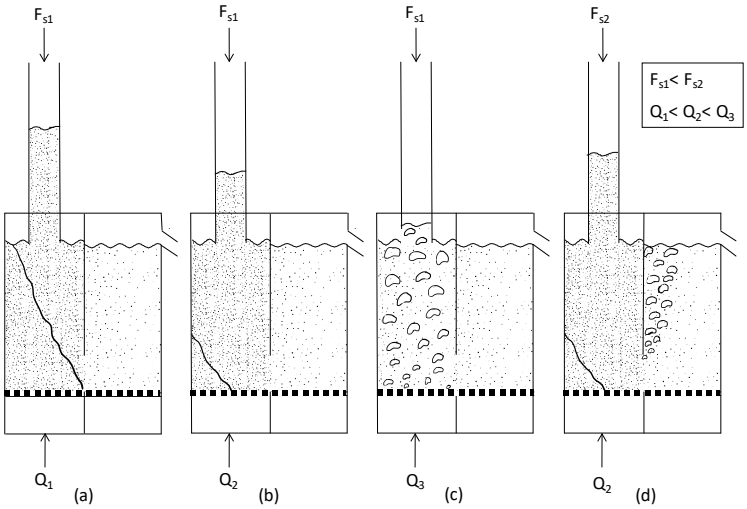

Fig. 4.5. Gas and solids flow patterns when aerating through the supply chamber for different aeration rates (Q_1, Q_2 and Q_3) and different solids flows (F_{s1} and F_{s2}).

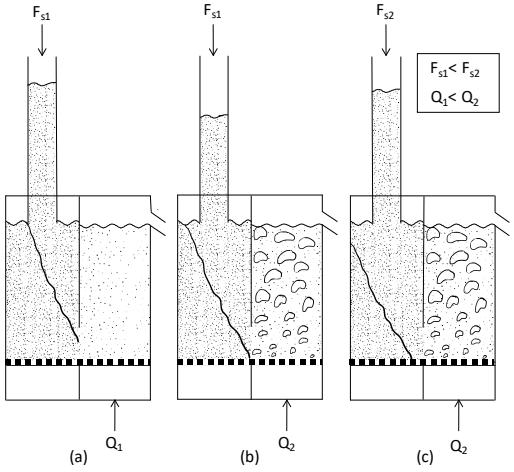

Fig. 4.6. Gas and solids flow patterns when aerating through the recycle chamber for different aeration rates (Q_1 and Q_2) and different solids flows (F_{s1} and F_{s2}).

The unexpected trends found when analyzing the pressure drop through the opening (Fig. 4.4(a)) are the result of the particular features of the gas-solids flows across the loop seal. It was demonstrated that the pressure drop through the opening is affected by the aeration mode and it does not follow a homogeneous gas-solids pattern. As a result, this pressure drop cannot be estimated as that between two fluidized beds [63], which is assumed by many authors [64,65]. Special features concerning the gas-solids flow through the opening in a loop seal unit are extensively assessed in [66].

The superior performance of the loop seal for controlling the solids circulation when aerated through the SC (Fig. 4.4(b)) is achieved due to the high resistance offered by the opening which, for a given aeration, leads to a higher circulation of gas through the SC. This results in a higher pressure

drop through the column of solids in the SC/downcomer and, therefore, along the riser in a solids circulating loop, entailing a higher solids flux. Feeding the same air flowrate through the RC leads to the lowest circulation of gas through the SC i.e., the lowest pressure drop and solids circulation. The best option when the stagnant zones are to be minimized is the aeration through both the SC and RC. If the loop seal is intended just as a solids circulation device, aerating through both chambers while keeping the SC under fluidized regime is the best option to reach the maximum solids flux, promoting a uniform and smoother gas-solids flow (see Section 4.3.2.1 for details on the operation of loop seals in CFB systems). It can be concluded that the lower the stagnant zones and gas-solids flow resistances the lower the loop seal ability to control the solids circulation in a CFB loop.

A proper model of the resistance to flow found by gas and solids in actual loop seals (as a function of the aeration) would allow to solve the model presented in Section 3.1.5. Special attention needs to be paid to the opening/horizontal passage, usually not considered in models [59,67,68], since it tends to be the limiting resistance, setting the gas and solids distribution in a loop seal device. In fact, it was neglected in the model in **Paper III**, although with minor implications when comparing with the measurements since the modelled ULS is out of the pressure loop (CFM at TU-Wien operates with a lower pipe connection).

Unfortunately, non-ideal gas-solids flow patterns occurring in actual loop seals cannot be addressed by simple semi-empirical 1D models. This explains why the models of loop seal in CFB and DFB are still based on empirical correlations, in general, difficult to apply out of the system in which they were obtained. To obtain a comprehensive description, CFD simulation appears to be the right way to predict the actual gas-solid flow if a new loop seal is to be designed. However, modelling of the gas-solid flow in the loop seal and the standpipe is still recognized as the bottle neck for the simulations of the whole CFB loop in the CFD scheme [69,70].

4.3.2. Loop seal coupled to a CFB unit

4.3.2.1. Control of solids circulation in a CFB unit

There are two statements that must be fulfilled at any CFB unit in which the solids circulation is intended to be controlled by the aeration in the loop seal: (i) the standpipe needs to be operated under moving bed flow and (ii) the entrainment in the riser needs to be sensitive to the solids inventory in the riser, i.e., from the design point of view,

(i) the cross section of the standpipe must be selected to allow that the superficial velocity of the solids, under the maximum operating solids flux, is below that of incipient fluidization
(ii) the riser must be designed to operate far from the saturation carrying capacity of the gas, considering the operative window of gas and solids velocities

In typical CFB boilers these requirements are rarely met since: the huge solids circulations imply solids velocities in the standpipes (usually an extension of the cyclone outlet, designed to meet the separation requirements) above that of incipient fluidization and, the height of the riser is to be maximized for allocating the water walls. Hence, the belief spread by boilers community about the limited ability of loop seals for controlling the solids circulation.

For a given aeration in the riser, as increasing the aeration in the loop seal, the gradient of pressure in the standpipe increases and the height of solids decreases due to the evacuation of material to satisfy the new pressure balance. If the riser is operated below the saturating carrying capacity, the solids flux increases with the increase in the solids inventory and pressure drop in the riser; otherwise the system reaches a new steady state with the same solids circulation but higher pressure. If the aeration in the loop seal is such that the standpipe is fluidized, the system operates with the minimum height of solids in the standpipe, maximum sealing pressure, maximum solids inventory in the riser, and so, maximum solids circulation. Under this operation, the resistance in the circulating device is minimum and the solids circulation can only be increased by increasing the aeration in the riser. In

a properly designed CFB unit the widest range of solids circulation control is obtained when combining both, the loop seal and riser aerations.

4.3.2.2. Extrapolating the performance of an isolated loop seal to that operating within a CFB unit

Note that in an isolated loop seal, as that used in this study (Fig. 4.1), setting a solids flux and an aeration flowrate, leads to a height of solids in the downcomer (i.e., solids inventory) and a pressure drop in the outlet valve (P_{15}-P_1, according to Fig. 4.1). Comparing the pressure balance of a given isolated loop seal with the same loopseal coupled to a riser in a CFB unit it is noticed that: the performance of an isolated loop seal under a given aeration flowrate and solids flux, can represent the operation of this loop seal unit coupled to a CFB system operating under the same solids flux and, in which the pressure drop of the riser and the cyclone is equal to pressure drop in the outlet valve.

Following this approach, the performance of an isolated loop seal can be characterized by experiments as those carried out in this work leading to a performance chart. Then, this chart can be used to obtain the aeration required in that loop seal when coupled to a CFB unit to achieve a given solids flux. Further discussion on this can be found in **Paper IV**-Section 4.2.2.

Chapter 6. Conclusions

Solar steam gasification of biomass is a highly attractive technology for generating biofuels with maximum share of renewable energy. The hybridization of gasification and solar energy allows taking the most of locations with moderate resources of both, biomass and solar irradiance.

This thesis proposes a new concept of biomass gasification assisted by solar thermal energy, as an extension of a state-of-the-art (no-solar) dual fluidized bed gasification (DFBG). Solid particles are used as thermal energy carrier, circulating between the solar receiver and the gasifier with intermediate thermal energy storage. The advantage of this configuration is that the solar receiver and the reactor are uncoupled, while thermal integration is highly efficient since carrier particles are directly used in the reactor (overcoming the practical problems that have buried the development of allothermal steam gasifiers up to now).

The solar steam gasification of biomass in DFBG was assessed by modelling. The best options for integrating the external solids circulation into the DFBG unit were identified. Moreover, results shown that char conversions of 70-80% in the gasification unit can be reached under char residence times of 20-30 min. This value is much higher than those reached in current (non-solar) DFBG, typically operated in the range of 1-5 min (10-30% char conversion). As a result, the gasification unit in SDFBG should be significantly modified to operate in solar mode. Adapting the design to allow the operation both, at autothermal and solar mode is another challenge to overcome in the new SDFBG.

A fluid-dynamic model of a conventional DFBG unit was developed and results were compared against experimental measurements from a cold flow model DFBG. The model was used to analyze the hydrodynamic limitations of the new proposed SDFBG. Results showed that typical solids inventories and solids fluxes required by an SDFBG can be achieved by increasing around three times the diameter of the gasification unit compared to that of a conventional DFBG. Moreover, the loop seal is identified as a key device for allowing the flexible operation of the SDFBG under different loads of external heat.

The importance of loop seal operation in a SDFBG motivated the experimental work carried out in a cold flow model to shed light on the operation of these units as non-mechanical valves. The gas split through the chambers of the loop seal was studied. It was concluded that the resistance offered by the horizontal passage joining the bottom of the SC and RC results in a non-homogeneous gas-

solids flow patterns which, ultimately, establishes the actual gas division through the chambers. These non-ideal gas-solids flow patterns cannot be addressed by simple semi-empirical 1D models; although CFD appears as a useful tool to predict the behavior of these units, a comprehensive generalization is difficult.

A flexible SDFBG able to operate both under autothermal and at high allothermal conditions was designed using the gained knowledge. The most advantageous integration options of the external solids circulation into the DFBG were considered, leading to different design and operation requirements. The designed SDFBG allows char conversions in the gasifier ranging from 15 to 80% under autothermal and high allothermal conditions, respectively and, leading to a maximum solar external heat of around 2.6 $MJ/kg_{bio,daf}$.

Overall, this study show that the proposed SDFBG presents huge scaled-up potential. Some modifications are needed compared with the current state-of-the-art technologies of DFBG, mainly: a wider gasifier unit, a narrower riser-combustor and a dedicated lower loop seal for adapting the operation to changes in external heat loads.

The proposed technology can be further improved by using a catalyst, alleviating the requirements in the gasifier. Moreover, the CO_2 capture in a gasifier-carbonator using Ca-based sorbents would allow even better benefits.

6.1. Future work

Although the modeling work made in this work was enough for the essential assessment of the technology performance, some improvements are necessary for a more quantitative description. From the modelling point of view, the prediction capability of the fluid-dynamics models of the riser and the loop seal should be improved. Although the hydrodynamics performance of the riser has received huge attention from the research community, most of model developed up to now are still semi-empirical and based either on CFB boilers or catalytic reactors, so they are not general enough to extrapolate to other units. The emerging fluidized bed technologies dealing with the reduction of CO_2 emission can be quite different from fluidized bed developed up to now, as demonstrated in this thesis with the SDFBG which is rather different compared to existing DFBGs. Therefore, since general model based on fundamental knowledge seems far, dedicated semi-empirical model for these specific unit are required for obtaining a more accurate prediction by modelling. On the other hand, it would be interesting to use the gained knowledge on the gas-solids flow patterns in loop seal devices for improving the prediction of model by using CFD.

Regarding the concept, it would be of special interest extending the study made in **Paper II** to consider the transient response of the process under changes in the solar resource/TES. Research on catalytic gasification is a good branch to explore for increasing the potential of the proposed technology allowing to process biomasses with lower char reactivities and/or reducing the required inventory of solids to attain high char conversion. Exploring other designs as a multi-stage gasification unit would be interesting as a way to increase the char conversion while keeping the required solids inventory. Moreover, char separation also appears as a good option for taking the most of the solar resource while reducing the required solids inventory in the gasification unit, but further research is still required to explore its effectiveness and application.

References

[1] T. Kodama, High-temperature solar chemistry for converting solar heat to chemical fuels, Prog. Energy Combust. Sci. 29 (2003) 567–597. https://doi.org/10.1016/S0360-1285(03)00059-5.

[2] G. Liu, E.D. Larson, T.G. Williams, Robert H. Kreutz, X. Guo, Making Fischer−Tropsch Fuels and Electricity from Coal and Biomass: Performance and Cost Analysis, Energy Fuels. 25 (2011) 415–437. https://doi.org/DOI:10.1021/ef101184e.

[3] R.W. Taylor, R. Berjoan, J.P. Coutures, Solar gasification of carbonaceous materials, Sol. Energy. 30 (1983) 513–525. https://doi.org/10.1016/0038-092X(83)90063-4.

[4] J.P. Murray, E.A. Fletcher, Reaction of steam with cellulose in a fluidized bed using concentrated sunlight, Energy. 19 (1994) 1083–1098. https://doi.org/10.1016/0360-5442(94)90097-3.

[5] G.J. Nathan, B.B. Dally, Z.T. Alwahabi, P.J. Van Eyk, M. Jafarian, P.J. Ashman, Research challenges in combustion and gasification arising from emerging technologies employing directly irradiated concentrating solar thermal radiation, Proc. Combust. Inst. 36 (2017) 2055–2074. https://doi.org/10.1016/j.proci.2016.07.044.

[6] T. Kodama, S. Bellan, N. Gokon, H.S. Cho, Particle reactors for solar thermochemical processes, Sol. Energy. 156 (2017) 113–132. https://doi.org/10.1016/j.solener.2017.05.084.

[7] A. Nzihou, G. Flamant, B. Stanmore, Synthetic fuels from biomass using concentrated solar energy - A review, Energy. 42 (2012) 121–131. https://doi.org/10.1016/j.energy.2012.03.077.

[8] G. Flamant, D. Gauthier, H. Benoit, J.L. Sans, R. Garcia, B. Boissière, R. Ansart, M. Hemati, Dense suspension of solid particles as a new heat transfer fluid for concentrated solar thermal plants: On-sun proof of concept, Chem. Eng. Sci. 102 (2013) 567–576. https://doi.org/10.1016/j.ces.2013.08.051.

[9] E.D. Gordillo, A. Belghit, A bubbling fluidized bed solar reactor model of biomass char high temperature steam-only gasification, Fuel Process. Technol. 92 (2011) 314–321. https://doi.org/10.1016/j.fuproc.2010.09.021.

[10] P. Guo, P.J. Van Eyk, W.L. Saw, P.J. Ashman, G.J. Nathan, E.B. Stechel, Performance assessment of Fischer-Tropsch liquid fuels production by solar hybridized dual fluidized bed gasification of lignite, Energy and Fuels. 29 (2015) 2738–2751. https://doi.org/10.1021/acs.energyfuels.5b00007.

[11] P. Guo, W.L. Saw, P.J. Van Eyk, E.B. Stechel, P.J. Ashman, G.J. Nathan, System Optimization for Fischer-Tropsch Liquid Fuels Production via Solar Hybridized Dual Fluidized Bed Gasification of Solid Fuels, Energy and Fuels. 31 (2017) 2033–2043. https://doi.org/10.1021/acs.energyfuels.6b01755.

[12] P. Xiao, L. Guo, X. Zhang, C. Zhu, S. Ma, Continuous hydrogen production by biomass gasification in supercritical water heated by molten salt flow: System development and reactor assessment, Int. J. Hydrogen Energy. 38 (2013) 12927–12937. https://doi.org/10.1016/j.ijhydene.2013.04.139.

[13] H. Wu, Q. Liu, Z. Bai, G. Xie, J. Zheng, B. Su, Thermodynamics analysis of a novel steam/air biomass gasification combined cooling, heating and power system with solar energy, Appl. Therm. Eng. 164 (2020) 114494. https://doi.org/10.1016/j.applthermaleng.2019.114494.

[14] M. Puig-Arnavat, E.A. Tora, J.C. Bruno, A. Coronas, State of the art on reactor designs for solar gasification of carbonaceous feedstock, Sol. Energy. 97 (2013) 67–84. https://doi.org/10.1016/j.solener.2013.08.001.

[15] S. Abanades, S. Rodat, H. Boujjat, Solar thermochemical green fuels production: A review of biomass pyro-gasification, solar reactor concepts and modelling methods, Energies. 14

(2021). https://doi.org/10.3390/en14051494.
[16] A.P. Bruckner, Continuous duty solar coal gasification system using molten slag and direct-contact heat exchange, Sol. Energy. 34 (1985) 239–247. https://doi.org/10.1016/0038-092X(85)90061-1.
[17] P.K. Falcone, Technical Review of the Solid Particle Receiver Program, United States, 1984. https://doi.org/https://doi.org/10.2172/6719789.
[18] P.K. Falcone, J.E. Noring, J.M. Hruby, Assessment of a solid particle receiver for a high temperature solar central receiver system, Energy Procedia. 49 (1985) 398–407.
[19] C.K. Ho, A review of high-temperature particle receivers for concentrating solar power, Appl. Therm. Eng. 109 (2016) 958–969. https://doi.org/10.1016/j.applthermaleng.2016.04.103.
[20] K. Jiang, X. Du, Y. Kong, C. Xu, X. Ju, A comprehensive review on solid particle receivers of concentrated solar power, Renew. Sustain. Energy Rev. 116 (2019) 109463. https://doi.org/10.1016/j.rser.2019.109463.
[21] L. Lundberg, Solid Fuel Conversion in Dual Fluidized Bed Gasification − Modelling and Experiments, PhD Thesis, Chalmers University of Technology, 2018.
[22] M.O. Adegboye, Continuous Segregation and Removal of Biochar from Bubbling Fluidized Bed, Master Thesis, The University of Western Ontario, 2013.
[23] B. Lv, Z. Luo, B. Zhang, X. Qin, X. Zhu, Particle motion and separation behavior of coal in gas–solid separation fluidized bed, Powder Technol. 339 (2018) 344–353. https://doi.org/10.1016/j.powtec.2018.08.013.
[24] S. Turn, C. Kinoshita, Z. Zhang, D. Ishimura, J. Zhou, An experimental investigation of hydrogen production from biomass gasification, Int. J. Hydrogen Energy. 23 (1998) 641–648. https://doi.org/10.1016/s0360-3199(97)00118-3.
[25] A. Gómez-Barea, B. Leckner, Estimation of gas composition and char conversion in a fluidized bed biomass gasifier, Fuel. 107 (2013) 419–431. https://doi.org/10.1016/j.fuel.2012.09.084.
[26] A. Gómez-Barea, B. Leckner, Modeling of biomass gasification in fluidized bed, Prog. Energy Combust. Sci. 36 (2010) 444–509. https://doi.org/10.1016/j.pecs.2009.12.002.
[27] L. Lundberg, D. Pallarès, H. Thunman, Upscaling Effects on Char Conversion in Dual Fluidized Bed Gasification, Energy and Fuels. 32 (2018) 5933–5943. https://doi.org/10.1021/acs.energyfuels.8b00088.
[28] J. Karl, T. Pröll, Steam gasification of biomass in dual fluidized bed gasifiers: A review, Renew. Sustain. Energy Rev. (2018). https://doi.org/10.1016/j.rser.2018.09.010.
[29] J. Corella, J.M. Toledo, G. Molina, A review on dual fluidized-bed biomass gasifiers, Ind. Eng. Chem. Res. 46 (2007) 6831–6839. https://doi.org/10.1021/ie0705507.
[30] P. Kaushal, T. Proell, H. Hofbauer, Application of a detailed mathematical model to the gasifier unit of the dual fluidized bed gasification plant, Biomass and Bioenergy. (2011). https://doi.org/10.1016/j.biombioe.2011.01.025.
[31] H. Hermann, R. Reinhard, B. Klaus, K. Reinhard, A. Christian, Biomass CHP Plant Güssing – A Success Story, Expert Meet. Pyrolysis Gasif. Biomass Waste. (2002).
[32] T. Pröll, C. Aichernig, R. Rauch, H. Hofbauer, Performance characteristics of an 8 MWth combined heat and power plant, in: 12th Int. Conf. Fluid. - New Horizons Fluid. Eng., 2007. https://doi.org/10.2202/1542-6580.1398.
[33] Agencia Andaluza de la Energía, Radiación Solar, (n.d.). http://www.agenciaandaluzadelaenergia.es/Radiacion/radiacion1.php (accessed December 1, 2019).
[34] P. Kaushal, T. Pröll, H. Hofbauer, Modelling and simulation of the biomass fired dual fluidized bed gasifier at Guessing/Austria, RE&PQJ. 1 (2007) 300–306.
[35] S. Kaiser, G. Lo, K. Bosch, H. Hofbauer, Hydrodynamics of a dual fluidized bed gasifier. Part II: simulation of solid circulation rate, pressure loop and stability, Chem. Eng. Sci. 58 (2003) 4215–4223. https://doi.org/10.1016/S0009-2509(03)00233-1.

[36] K. Bosch, Scale UP der Dampf- Wirbelschicht- Biomassevergasung, PhD Thesis, Vienna University of Technology, 2007.
[37] R. Darton, R. LaNauze, J. Davidson, D. Harrison, Bubble growth due to coalescence in fluidised beds, Powder Technol. 68 (1991) 117–123.
[38] F. Johnsson, S. Andersson, B. Leckner, Expansion of a freely bubbling fluidized bed, Powder Technol. 68 (1991) 117–123. https://doi.org/10.1016/0032-5910(91)80118-3.
[39] M. Streat, K.C. Wilson, Comments on moving-bed solids flow between two fluidized beds, Powder Technol. 24 (1979) 271–272. https://doi.org/10.1016/0032-5910(79)87046-1.
[40] X. Yang, Z. Ma, Z. Liang, H. Chen, J. Wang, Hydrodynamic characteristics in a cold model of the dual fluidized bed with mixed particles, Powder Technol. 351 (2019) 291–304. https://doi.org/10.1016/j.powtec.2019.04.015.
[41] P. Bareschino, R. Solimene, R. Chirone, P. Salatino, Gas and solid flow patterns in the loop-seal of a circulating fluidized bed, Powder Technol. 264 (2014) 197–202. https://doi.org/10.1016/j.powtec.2014.05.036.
[42] G. Löffler, S. Kaiser, K. Bosch, H. Hofbauer, Hydrodynamics of a dual fluidized-bed gasifier — Part I : simulation of a riser with gas injection and diffuser, Chem. Eng. Sci. 58 (2003) 4197–4213. https://doi.org/10.1016/S0009-2509(03)00232-X.
[43] D. Pallarès, F. Johnsson, Macroscopic modelling of fluid dynamics in large-scale circulating fluidized beds, Prog. Energy Combust. Sci. 32 (2006) 539–569. https://doi.org/10.1016/j.pecs.2006.02.002.
[44] D. Kunii, Entrainment of Solids from Fluidized Beds I. Hold-Up of Solids in the Freeboard II. Operation of Fast Fluidized Beds, Powder Technol. 61 (1990) 193–206.
[45] F. Johnsson, Vertical distribution of solids in a CFB-Furnace, in: 13th Int. Conf. Fluid. Bed Combust., Orlando, 1995.
[46] T. Djerf, Solids Flow in Large-Scale Circulating Fluidized Bed Furnaces, PhD Thesis, Chalmers University of Technology, 2021.
[47] W.K. Lewis, E.R. Gilliland, P.M. Lang, Entrainment from fluidized beds, Chem. Eng. Prog. Symp. Ser. (1962) 58–65.
[48] D. Kunii, O. Levenspiel, Fluidization Engineering, 2nd ed., Butterworth-Heinemann, Stoneham, 1992. https://doi.org/10.1016/b978-0-7506-9236-6.50001-9.
[49] J.F. Davidson, Circulating fluidised bed hydrodynamics, Powder Technol. 113 (2000) 249–260.
[50] M.J. Rhodes, D. Geldart, A Model for the Circulating Fluidized Bed, Powder Technol. 53 (1987) 155–162.
[51] C.Y. Wen, L.H. Chen, Fluidized Bed Freeboard Phenomena: Entrainment and Elutriation, AlChE J. 28 (1982) 117–128.
[52] J. Kotik, T. Pröll, H. Hofbauer, Advanced concept for a “next generation” biomass gasification CHP-plant-Basic engineering and cold flow model results, in: Circ. Fluid. Bed Technol. IX, Hamburg, 2008.
[53] S. Yang, H. Yang, H. Zhang, J. Li, G. Yue, Impact of operating conditions on the performance of the external loop in a CFB reactor, Chem. Eng. Process. Process Intensif. 48 (2009) 921–926. https://doi.org/10.1016/j.cep.2008.12.004.
[54] F. Oliveira, G.H. Santos Furquim, V.O. Ochoski Machado, M.R. Parise, J. Ramírez Bahainne, Operational Influence of the Mono-Chamber Aeration Mode in the Loop Seal of a Circulating Fluidized Bed, Lat. Am. Appl. Res. 51 (2021) 15–20. https://doi.org/10.52292/j.laar.2021.181.
[55] X. Han, Z. Cui, X. Jiang, J. Liu, Regulating characteristics of loop seal in a 65 t/h oil shale-fired circulating fluidized bed boiler, Powder Technol. 178 (2007) 114–118. https://doi.org/10.1016/j.powtec.2007.04.015.
[56] S.W. Kim, S.D. Kim, D.H. Lee, Pressure balance model for circulating fluidized beds with a loop-seal, Ind. Eng. Chem. Res. 41 (2002) 4949–4956. https://doi.org/10.1021/ie0202571.

[57] A. Chinsuwan, A mathematical model for predicting the flow behavior through a CFB reactor U type loop - seal, Int. J. Heat Mass Transf. 177 (2021). https://doi.org/10.1016/j.ijheatmasstransfer.2021.121541.

[58] E. Botsio, P. Basu, Experimental investigation into the hydrodynamics of flow of solids through a loop seal recycle chamber, Can. J. Chem. Eng. 83 (2005) 554–558. https://doi.org/10.1002/cjce.5450830319.

[59] C. Li, H. Li, Q. Zhu, A hydrodynamic model of loop-seal for a circulating fluidized bed, Powder Technol. 252 (2014) 14–19. https://doi.org/10.1016/j.powtec.2013.10.029.

[60] Y. Li, Y. Lu, F. Wang, K. Han, W. Mi, X. Chen, P. Wang, Behavior of gas-solid flow in the downcomer of a circulating fluidized bed reactor with a V-valve, Powder Technol. 91 (1997) 11–16. https://doi.org/10.1016/S0032-5910(96)03226-3.

[61] X. Yao, H. Yang, H. Zhang, C. Zhou, Q. Liu, G. Yue, Gas-solid flow behavior in the standpipe of a circulating fluidized bed with a loop seal, Energy and Fuels. 25 (2011) 246–250. https://doi.org/10.1021/ef1011897.

[62] P. Wang, J. Lu, W. Xing, H. Yang, M. Zhang, Impact of loop seal structure on gas solid flow in a CFB system, Powder Technol. 264 (2014) 177–183. https://doi.org/10.1016/j.powtec.2014.04.037.

[63] M. Kuramoto, D. Kunii, T. Furusawa, Flow of dense fluidized particles through an opening in a circulation system, Powder Technol. 47 (1986) 141–149. https://doi.org/10.1016/0032-5910(86)80110-3.

[64] L. Cheng, P. Basu, Effect of pressure on loop seal operation for a pressurized circulating fluidized bed, Powder Technol. 103 (1999) 203–211. https://doi.org/10.1016/S0032-5910(99)00018-2.

[65] P. Gao, Z. Tang, Y. Han, E. Li, X. Zhang, A pressure drop model of U-typed reduction chamber for iron ore suspension roasting, Powder Technol. 343 (2019) 255–261. https://doi.org/10.1016/j.powtec.2018.11.020.

[66] P. Basu, J. Butler, Studies on the operation of loop-seal in circulating fluidized bed boilers, Appl. Energy. 86 (2009) 1723–1731. https://doi.org/10.1016/j.apenergy.2008.11.024.

[67] C. Li, Z. Zou, H. Li, Q. Zhu, A hydrodynamic model of loop seal with a fluidized standpipe for a circulating fluidized bed, Particuology. 36 (2018) 50–58. https://doi.org/10.1016/j.partic.2017.02.005.

[68] Z. Tang, Y. Han, P. Gao, F. Yang, K. Xu, Y. Feng, A hydrodynamic model of U-type reduction chamber for iron ore suspension roaster, Powder Technol. 393 (2021) 441–448. https://doi.org/10.1016/j.powtec.2021.08.004.

[69] Q. Wang, H. Yang, P. Wang, J. Lu, Q. Liu, H. Zhang, L. Wei, M. Zhang, Application of CPFD method in the simulation of a circulating fluidized bed with a loop seal Part I-Determination of modeling parameters, Powder Technol. 253 (2014) 814–821. https://doi.org/https://doi.org/10.1016/j.powtec.2013.11.041.

[70] Q. Wang, H. Yang, P. Wang, J. Lu, Q. Liu, H. Zhang, L. Wei, M. Zhang, Application of CPFD method in the simulation of a circulating fluidized bed with a loop seal Part II-Investigation of solids circulation, Powder Technol. 253 (2014) 822–828. https://doi.org/10.1016/j.powtec.2013.11.040.

[71] M. Morin, L. Raynal, S.B.R. Karri, R. Cocco, Effect of solid loading and inlet aspect ratio on cyclone efficiency and pressure drop: Experimental study and CFD simulations, Powder Technol. 377 (2021) 174–185. https://doi.org/10.1016/j.powtec.2020.08.052.

[72] H. Hofbauer, R. Rauch, Stoichiometric Water Consumption of Steam Gasification by the FICFB-Gasification Process, in: Prog. Thermochem. Biomass Convers., 2008. https://doi.org/10.1002/9780470694954.ch14.

[73] C. Pfeifer, J. Schmid, T. Pröll, H. Hofbauer, Next generation biomass gasifier, in: 19th Eur. Biomass Conf. Exhib. Berlin, Ger., 2011.

[74] M. Barrio, B. Gøbel, H. Rimes, U. Henriksen, J.E. Hustad, L.H. Sørensen, Steam Gasification of Wood Char and the Effect of Hydrogen Inhibition on the Chemical Kinetics,

Prog. Thermochem. Biomass Convers. (2008) 32–46. https://doi.org/10.1002/9780470694954.ch2.

[75] M. Hemati, C. Laguerie, Détermination de la cinétique de vapogazéification de charbon de bois en thermobalance, Entropie. 142 (1988) 29–40.

[76] T. Kojima, P. Assavadakorn, T. Furusawa, Measurement and evaluation of gasification kinetics of sawdust char with steam in an experimental fluidized bed, Fuel Process. Technol. 36 (1993) 201–207. https://doi.org/10.1016/0378-3820(93)90028-3.

[77] A. Bhat, J. V. Ram Bheemarasetti, T. Rajeswara Rao, Kinetics of rice husk char gasification, Energy Convers. Manag. 42 (2001) 2061–2069. https://doi.org/10.1016/S0196-8904(00)00173-4.

[78] R.L. Hirsch, J.E. Gallagher, R.R. Lessard, R.D. Wesselhoft, Catalytic coal gasification: An emerging technology, Science (80-.). 215 (1982) 121–127. https://doi.org/10.1126/science.215.4529.121.

[79] NETL, Great Point Energy, Gasifipedia. (2017). https://www.netl.doe.gov/research/coal/energy-systems/gasification/gasifipedia/gpe (accessed February 11, 2022).

[80] P. Nanou, Biomass gasification for the production of methane, Univ. Twente. (2013) 173. http://purl.org/utwente/doi/10.3990/1.9789036535434.

Appendix A. Assessment of the LLS model error

As detailed in Section 5.2.1, the LLS was modelled assuming that the RC always operates under incipient fluidization while the gas velocity in the SC is adjusted to balance the pressure of the system. In this way the total amount of gas fed to the loop seal was calculated by the model. In the actual operation of a loop seal device the RC is not always at incipient fluidization, so the total fed gas flowrate for a required gas velocity in the SC cannot be directly calculated.

In the SDFBG designed for operating under C1, the cross section of the SC is narrower than that of the riser ($A_{SC,LLS}/A_{riser} = 0.5$) and, the required pressure drop in the SC, for all the SEH range, is given by the velocity of the solids against a stagnant gas. On the contrary, in the SDFBG designed for operating under C2, the solids velocity is constant for all the SEH range and, therefore, the gas velocity through the SC of the LLS needs to be adjusted to meet the pressure balance of the unit. Moreover, due to the large solids circulation, in this unit, the cross section of the SC is larger than that of the riser ($A_{SC,LLS}/A_{riser} = 3.4$).

In both cases the higher error induced by the assumptions made in LLS model takes place when operating under autothermal conditions since, as shown in Fig. 5.6(c) this operation requires the highest pressure drop through the SC (to compensate the decrease in the solids inventory in the gasifier), i.e., that requiring the highest gas flowrate in the LLS.

The potential error introduced by the model was assessed by increasing the gas circulating through the RC (considering the expansion of the bed) for the required gas in the SC under SEH=0 both, for C1 and C2. The gas velocity in the riser (which accounts for that coming from the RC) is calculated by the model as that required both, for entraining the solids and burning the char. Therefore, as increasing the gas circulating through the RC, the air fed through the bottom of the riser is reduced. The aeration in the riser can be compensated by that of the RC while keeping enough oxygen for the char combustion (considering that the air fed to the LLS is steam). The latter assumption implies that the introduction of part of the gas through the recycle pipe has a minor effect on the entrainment in the riser. Under these considerations, the velocity in the RC can be up to 10 times that of minimum fluidization in C1 and, 3 times in C2 due to the larger SC.

Note that these estimations are just useful to have an idea on how to work out the problem. Feeding air instead of steam in the LLS is another option for the operation under C1 where the gas is stagnant in the SC (i.e., there is no air flowrate upwards to the gasifier); it does not work for C2 where there is a net flow of gas upwards to the gasifier. Overall, it can be concluded that there is enough room to absorb the uncertainties given by the fluid-dynamics of the loop seal and that the conclusions of the study still state.